Icarus 311 (2018) 1–22

Contents lists available at ScienceDirect

Icarus

journal homepage: www.elsevier.com/locate/icarus

On deviations from free-radial outflow in the inner coma of comet 67P/Churyumov–Gerasimenko

S.-B. Gerig[a,*], R. Marschall[o], N. Thomas[a], I. Bertini[b], D. Bodewits[c], B. Davidsson[d], M. Fulle[e], W.-H. Ip[f], H.U. Keller[g], M. Küppers[h], F. Preusker[i], F. Scholten[i], C.C. Su[j], I. Toth[k], C. Tubiana[l], J.-S. Wu[j], H. Sierks[l], C. Barbieri[m], P.L. Lamy[n], R. Rodrigo[o,p], D. Koschny[q], H. Rickman[r], J. Agarwal[l], M.A. Barucci[s], J.-L. Bertaux[n], G. Cremonese[t], V. Da Deppo[u], S. Debei[b], M. De Cecco[v], J. Deller[l], S. Fornasier[s], O. Groussin[w], P.J. Gutierrez[x], C. Güttler[l], S.F. Hviid[i], L. Jorda[w], J. Knollenberg[i], J.-R. Kramm[l], E. Kührt[i], L.M. Lara[x], M. Lazzarin[m], J.J. Lopez Moreno[x], F. Marzari[m], S. Mottola[i], G. Naletto[m,b], N. Oklay[i], J.-B. Vincent[i]

[a] Physikalisches Institut, University of Bern, Sidlerstr. 5, CH-3012 Bern, Switzerland
[b] Centro di Ateneo di Studi ed Attivitá Spaziali, "Giuseppe Colombo" (CISAS), University of Padova, Via Venezia 15, 35131 Padova, Italy
[c] Department of Astronomy, University of Maryland, Atlantic Building, 4254 Stadium Drive, College Park, MD 20742-2421, USA
[d] Jet Propulsion Laboratory, M/S 183–401, 4800 Oak Grove Drive, Pasadena, CA 91109, USA
[e] INAF – Osservatorio Astronomico, Via Tiepolo 11, 34014 Trieste, Italy
[f] Graduate Institute of Astronomy, National Central University, 300 Chung-Da Rd, Chung-Li 32054, Taiwan
[g] Institute for Geophysics and Extraterrestrial Physics, TU Braunschweig, Mendelssohnstr. 3, 38106 Braunschweig, Germany
[h] Science Operations Department, European Space Astronomy Centre/ESA, P.O. Box 78, 28691 Villanueva de la Canada, Madrid, Spain
[i] Institut für Planetenforschung, Deutsches Zentrum für Luft- und Raumfahrt (DLR), Rutherfordstraße 2, 12489 Berlin, Germany
[j] Department of Mechanical Engineering, National Chiao Tung University, 1001 Ta-Hsueh Road, Hsinchu 30010, Taiwan
[k] MTA CSFK Konkoly Observatory of the Hungarian Academy of Sciences Budapest, Konkoly Thege M. ut 15–17. H1121 Budapest, Hungary
[l] Max-Planck-Institut für Sonnensystemforschung, Justus-von-Liebig-Weg, 3, 37077 Göttingen, Germany
[m] Department of Physics and Astronomy, University of Padova, Vicolo dell'Osservatorio 3, 35122 Padova, Italy
[n] Laboratoire Atmosphères, Milieux et Observations Spatiales, CNRS & Université de Versailles Saint-Quentin-en-Yvelines, Guyancourt, France
[o] International Space Science Institute, Hallerstraße 6, 3012 Bern, Switzerland
[p] Centro de Astrobiología, CSIC-INTA, European Space Agency (ESA), European Space Astronomy Centre (ESAC), PO Box 78, 28691 Villanueva de la Canada, Madrid, Spain
[q] Scientific Support Office, European Space Agency, 2201 Noordwijk, The Netherlands
[r] PAS Space Research Center, Bartycka 18A, PL-00716 Warszawa, Poland
[s] Observatoire de Paris, PSL Research University, CNRS, Univ. Paris Diderot, Sorbonne Paris Cité, UPMC Univ. Paris 06, Sorbonne Universités, 5 place Jules Janssen, 92195 Meudon, France
[t] INAF, Osservatorio Astronomico di Padova, Vicolo dell'Osservatorio 5, 35122 Padova, Italy
[u] CNR-IFN UOS Padova LUXOR, Via Trasea, 7, 35131 Padova, Italy
[v] UNITN, Universitá di Trento, Via Mesiano, 77, 38100 Trento, Italy
[w] Laboratoire d'Astrophysique de Marseille, 38 Rue de Frédéric Joliot-Curie, 13388 Marseille Cedex 13, France
[x] Instituto de Astrofisica de Andalucía (CSIC), c/ Glorieta de la Astronomía s/n, 18008 Granada, Spain

ARTICLE INFO

Article history:
Received 18 August 2017
Revised 6 March 2018
Accepted 8 March 2018
Available online 13 March 2018

ABSTRACT

The Optical, Spectroscopic, and Infrared Remote Imaging System (OSIRIS) onboard the European Space Agency's Rosetta spacecraft acquired images of comet 67P/Churyumov–Gerasimenko (67P) and its surrounding dust coma starting from May 2014 until September 2016. In this paper we present methods and results from analysis of OSIRIS images regarding the dust outflow in the innermost coma of 67P. The aim is to determine the global dust outflow behaviour and place constraints on physical processes affecting particles in the inner coma. We study the coma region right above the nucleus surface, spanning from the nucleus centre out to a distance of about 50 km comet centric distance (approximately 25 average comet radii). We primarily adopt an approach used by Thomas and Keller (1990) to study the dust outflow. We present the effects on azimuthally-averaged values of the dust reflectance of non-radial

* Corresponding author.
E-mail address: selina-barbara.gerig@space.unibe.ch (S.-B. Gerig).

https://doi.org/10.1016/j.icarus.2018.03.010

Keywords:
Rosetta
OSIRIS
67P/Churyumov–Gerasimenko
Inner coma
Dust

flow and non-point-source geometry, acceleration of dust particles, sublimation of icy dust particles after ejection from the surface, dust particle fragmentation, optical depth effects and the influence of gravitationally bound particles. All of these physical processes could modify the observed distribution of light scattered by the dust coma.

In the image analysis, profiles of azimuthally averaged dust brightness as a function of impact parameter b (azimuthal average, "Ā-curve") were fitted with a simple function that best fits the shape of our profile curves ($f(b; u, v, w, z) = u/b^v + wb + z$). The analytical fit parameters (u, v, w, z), which hold the key information about the dust outflow behaviour, were saved in a comprehensive database.

Through statistical analysis of these information, we show that the spatial distribution of dust follows free-radial outflow behaviour (i.e. force-free radial outflow with constant velocity) beyond distances larger than ∼11.9 km from the comet centre, which corresponds to a relative distance of about 6 average comet radii from the comet centre. Hence, we conclude that beyond this distance, and on average, fragmentation and gravitationally bound particles are negligible processes in determining the optically scattered light distribution in the innermost coma. Closer to the nucleus we observe dust outflow behaviour that deviates from free-radial outflow.

A comparison of our result profiles with numerical models using a Direct Simulation Monte Carlo (DSMC) approach with dust particle distributions calculated using a test particle approach has been used to demonstrate the influence of a complex shape and particle acceleration on the azimuthal average profiles. We demonstrate that, while other effects such as fragmentation or sublimation of dust particles cannot be ruled out, acceleration of the dust particles and effects arising from the shape of the irregular nucleus (non-point source geometry) are sufficient to explain the observed dust outflow behaviour from image data analysis.

As a by-product of this work, we have calculated "Afρ" values for the 1/r regime. We found a peak in the coma activity in terms of Afρ (normalised to a phase angle of 90°) of ∼210 cm 20 days after perihelion. Furthermore, based on simplified models of particle motion within bound orbits, it is shown that limits on the total cross-sectional area of bound particles might be derived through further analysis. An example is given.

1. Introduction

The scattering of sunlight by dust provides a means of studying processes in the inner comae of comets. The scattered light in the optical is relatively bright (comparable to the brightness of the nucleus itself in the case of comet 1P/Halley during the Giotto flyby - see Keller et al., 1994) and can be observed by high spatial resolution imaging systems (Szego et al., 1989). Dust emitted from the surface of a comet is accelerated by gas drag (Gombosi et al., 1985; Crifo and Rodionov, 1997). Hence, the dust traces, albeit in a complex way, the flow of gas from the nucleus. Modelling of this flow in 3D is now becoming increasingly common (Tenishev et al., 2008; Marschall et al., 2016). This is helpful in studying gas sources on the nucleus because the parent molecules in the gas are only observable through emission bands outside the visible wavelength range and are much fainter requiring monitoring instruments to have lower spatial resolution and/or lower temporal resolution than imaging systems (cf. for example Keller et al., 2007, Coradini et al., 2007 and Gulkis et al., 2007).

For the dust itself, the size distribution, the composition, the structure and its evolution once released from the nucleus are all of interest. Sizes may be such that the emission and drag processes are insufficient for the particles to reach escape velocity (Möhlmann, 1994; Crifo et al., 2005; Thomas et al., 2015; Fulle et al., 2016; Agarwal et al., 2016). Fragmentation of particles might occur as a result of imparted stresses (Thomas and Keller, 1990) and sublimation can result from the heating that occurs after particles have been emitted (Lien, 1990; Gicquel et al., 2016). In addition, the acceleration of the particle is related to the ratio of the cross-sectional area to the mass. Hence, detailed study of dust particle dynamics is an important part of the study of the innermost coma.

The purpose of this paper is to investigate the inner dust coma of 67P/Churyumov–Gerasimenko using a technique first elaborated by Thomas and Keller (1990) in which conservation of radiance (as a proxy for dust column density) on concentric surfaces is used to assess whether specific processes are dominant. We shall be referring to deviations from "1/r dependence" of the scattered brightness from the dust along a line-of-sight that would be expected for force-free radial outflow. Previous papers (Lin et al., 2015; Gicquel et al., 2016) have presented non 1/r dependencies in dust profiles of 67P. However, non-radial outflow, inhomogeneity of the source and the finite size of the source, all complicate the interpretation. Here, we address the question of when the dust outflow can be considered to be 1/r and use models to show potential explanations for observed deviations from 1/r close to the nucleus.

In Section 2, we will re-iterate and expand upon the technique used by Thomas and Keller (1990) which includes the definition of a quantity we refer to as the "azimuthal average" and which is related to the commonly used definition of "Afρ" (A'Hearn et al. 1984). This relationship will be derived in Section 4.3. Given the apparent dominance of large slow moving particles in the inner coma of 67P (Fulle et al., 2015), we also provide an assessment of the influence of these particles on the azimuthal average. In Section 3, we will describe the construction of a database of OSIRIS images in which quantities such as azimuthal average values at different impact parameters are fit and tabulated. In Section 4, this database will be analysed in different ways to provide insight into the processes involved. We end with a short conclusions and discussion section.

2. The azimuthal average and its interpretation

2.1. Force-free radial outflow

The simplest model of the dust coma is the free-radial outflow/point source approximation. In this model dust particles are assumed to be released isotropically from a central point-source at a constant velocity ignoring acceleration. The local dust density

can then be written as

$$n_d(r) = \frac{Q_d}{4\pi r^2 v_d} \quad (1)$$

where Q_d is the dust production rate, v_d is the velocity of the outflow and r is the distance from the point source. Integration of this equation along the line of sight (± infinity) produces a column density,

$$N_d(b) = \frac{Q_d}{4bv_d} \quad (2)$$

where b is the impact parameter – the distance to the nucleus in the image plane passing through the centre of the nucleus.

Under the assumption that particles are not modified in any way, the radiance from the dust is proportional to the observed column density. This clearly shows that imaging observations of dust emission from a point source should produce radial profiles that vary in brightness with 1/b. (In the literature, this is usually referred to as a "1/r dependence" but we are using r here for distances to the nucleus in 3D whereas in the above equation b is the impact parameter. The vectorial distance to the nucleus will not be used further herein and we shall refer to deviations from a "1/r law" in the text for clarity while using the symbol, b, for the impact parameter within formulae.) This approximation still holds in the event that emission of the dust has an angular dependency which one would normally expect to be the case for insolation-driven emission (i.e. emission roughly proportional to the cosine of the solar zenith angle).

Clearly, v_d cannot be constant throughout the inner coma because the dust particles must be accelerated from rest at the surface of the nucleus to velocities well in excess of escape velocity. The gas itself is also accelerating. The computations of Gombosi et al. (1985) showed that dust terminal velocities could easily exceed 200 m/s because of gas drag and these velocities are particle size dependent (Davidsson et al., 2010). As such, v_d in Eqs. (1) and (2) is size dependent and the local density and column density then become integrals over particle size. Inspection of Eq. (2) shows that, after emission from the surface, the local dust density must drop more steeply than a "1/r law" in the acceleration region and thus investigation of the inner coma of comet 1P/Halley was targeted at looking for this behaviour in the inner coma. In this case, it was shown (Thomas and Keller, 1990) that the scattered light from the dust did indeed tend towards 1/r at distances greater than 50 km from the nucleus or in other words for distances >10 average Halley-radii. (The average Halley-radius of 5 km was chosen such that a sphere with the mentioned radius has about the same surface area as the nucleus of comet Halley, which was for this purpose approximated by an ellipsoidal shape following Keller et al. (1994)). However, directly above the nucleus, profiles of the conserved quantity, $I{\cdot}b$ (see Section 2.2), where I is the radiance from the dust column, dropped when approaching the nucleus surface instead of rising. This was recognized (Huebner et al., 1988; Reitsema et al., 1989) as being the result of the finite size of the source. This was also discussed extensively by Boice et al. (2002) in relation to observations of comet 19P/Borrelly with the Deep Space 1 spacecraft. The specification of the point where $b = 0$ as the emitting surface was seen as being a contributor to this problem because the source has a finite size. In the approximation of Eq. (1), n goes to infinity as b goes to zero. Even at this time it was recognized that there seems to be no physical way to define the value of b at the emitting surface.

2.2. The azimuthal average

The idea of defining a surface through which the dust would pass and thereby applying conservation of scattering area was first discussed in Thomas and Keller (1990). According to a formulation of Gauss' theorem

$$\int \boldsymbol{E} \cdot \boldsymbol{dS} = constant$$

a flux $\boldsymbol{E}$ integrated over an arbitrary closed surface around a finite source multiplied by the surface area (surface element $\boldsymbol{dS}$) is constant. The value of the integral gives the source strength of the enclosed source. It was shown by Thomas and Keller (1990) that observed reflectance from imaging data can be related to a dust flux and that in the case of line-of-sight observations integrations over cylindrical surfaces enclosing a source (i.e. the comet nucleus) are a good approximation for closed surfaces. In other words, in the free radial outflow/point source approximation, the integral of the column density along the length of a circle of circumference, d ($= 2\pi b$), centred on the source is a constant independent of the size of the circle. This can be written in terms of angle as

$$A(b) = k\int_0^{2\pi} N(b,\theta)d\theta = k\int_0^{2\pi} \frac{Q(\theta)}{4bv_d(\theta)}d\theta \quad (3)$$

where k is a constant of proportionality that can be used to convert the column density into an observed radiance or a reflectance and

$$A(b)\ b = constant = 2\pi\bar{A}. \quad (4)$$

The quantity $A(b)$ is an azimuthally integrated dust reflectance and the quantity $\bar{A} = Ab/2\pi$, was referred to as the azimuthal average by Thomas and Keller and has dimensions of $[m]$ if A is in reflectance units. The product of reflectance and impact parameter is closely related to the definition of Afρ (A'Hearn et al., 1984) as will be shown in Section 4.3.

This approach effectively eliminates the principal issue with radial profiles, namely the impossibility of defining a 1D profile taking into account intersecting dust flows and non-radial expansion of the dust into 3D, and the problem with defining the distance at the emitting surface. Here, the source is completely surrounded by a cylindrical surface (taking into account the line of sight) so that the entire dust flux passes through the surface as the dust expands with constant velocity into the inner coma. We are in effect applying an equation of continuity. In the following data analysis, we are interested in deviations from the constancy of the azimuthal average which we expect for free-radial outflow and we discuss the physical processes that could explain the observed deviations.

2.3. Illustration using a simple model calculation

Some of the important aspects mentioned above (e.g. the effect of acceleration on the azimuthal average) can be seen clearly in simplified numerical models. We use these models to illustrate the basic physics of the problem. A more detailed description of our numerical models is given in Section 5.

Fig. 1 shows a calculation of isotropic gas outflow in a spherically symmetric system. The gas velocities and densities have been computed using the Direct Simulation Monte Carlo (DSMC) technique. (Cercignani, 2000 discusses analytical solutions to this problem but we merely use the numerical approach here as a starting point before adding further complexity.) The gas density has then been converted into gas column density. Fig. 2 shows the behaviour of an integral of the gas column density, multiplied by b in this case, showing, as expected, the value asymptotically approaching a constant value from higher values close to the nucleus.

To relate directly the distances in the coma to the size of the central object, a relative distance coordinate is introduced as the ratio of impact parameter to object radius b/R We will use an average radius of $\bar{R} = 2$ km to define the relative distance coordinate for comet 67P. The average radius was chosen such that the surface area of a spherical nucleus with radius $\bar{R}$ is about the same

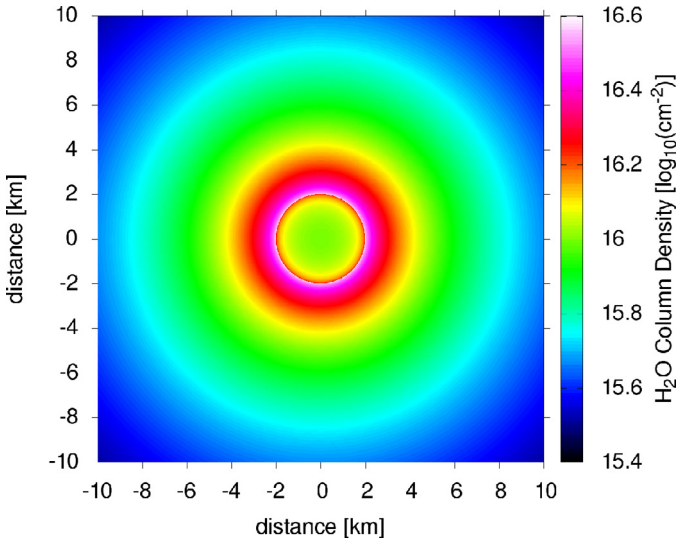

Fig. 1. The column density through a spherically symmetric outflow of water vapour from a simulated, spherical nucleus of 2 km in radius computed using the Direct Simulation Monte Carlo (DSMC) technique.

as the surface area of the irregular nucleus itself. This more general formulation allows easier comparison of the dust outflow for different sized comets (e.g. comet Halley and comet Churyumov–Gerasimenko).

For completeness, we also show computations for the dust in this simple case using a standard analytical approach for the drag. The acceleration of the dust in the gas flow field is computed taking into account the gas drag through a standard drag equation and the gravity field from the sphere

$$m\boldsymbol{a} = \boldsymbol{F}_G + \frac{1}{2} C_D m_g n_g \sigma |\boldsymbol{v}_g - \boldsymbol{v}_d| (\boldsymbol{v}_g - \boldsymbol{v}_d) \tag{5}$$

where the drag coefficient (usually set to 2 for smooth spheres) is here set through the equation

$$C_D = \frac{2s^2+1}{\sqrt{\pi} s^3} e^{-s^2} + \frac{4s^4+4s^2-1}{2s^4} \mathrm{erf}(s) + \frac{2(1-\varepsilon)\sqrt{\pi}}{3s} \sqrt{\frac{T_d}{T_g}} \tag{6}$$

where

$$s = \frac{|\boldsymbol{v}_g - \boldsymbol{v}_d|}{\sqrt{\frac{2kT_g}{m_g}}} \,. \tag{7}$$

The other variables in Eqs. (5) and (6) are the molecular mass of the gas (m_g), the local density (n_g), the cross-section (σ), the fraction of specular reflection (ε) (set to 0), and the gas and dust velocities ($\boldsymbol{v}_g$, $\boldsymbol{v}_d$) which provide part of the force on the dust particle ($m\boldsymbol{a}$). The gas temperature (T_g) is taken from the DSMC simulation of the gas flow field and we assume the dust and gas to be in thermal equilibrium (dust temperature $T_d = T_g$). The gravitational accelerations at the dust particle positions were calculated for a central sphere with radius 2 km and a bulk density of 462 kg/m^3 and a constant density of 440 kg/m^3 for spherical dust particles was assumed.

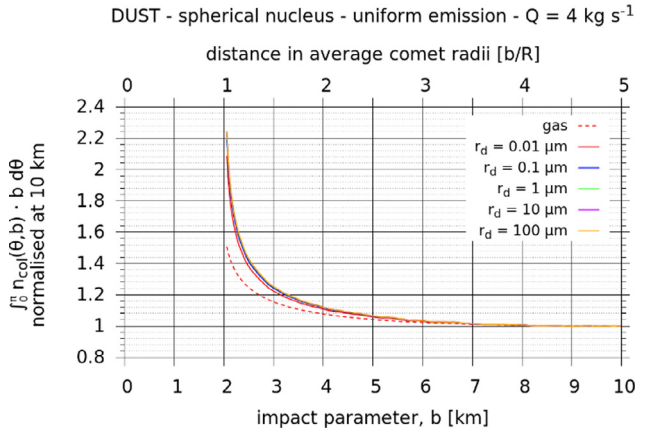

Fig. 3. The azimuthal average for different dust particle sizes follows a similar trend to that of the gas. The differences between the different particle sizes are rather small in this case.

In Fig. 3, we have computed the value of $\bar{A}$ but normalised to 1 at 10 km distance from the nucleus centre. Evaluating Eq. (2) with acceleration modifying the dust velocity v_d above the surface of the nucleus, the local dust density must drop more steeply than a "1/r-law". We observe this drop in our simulation result and because in this case we only take into account particle acceleration caused by gas drag and gravity, this shows the expected behaviour as a result of acceleration only. At the limb of the spherical nucleus (2 km from the origin), the azimuthal average is at a maximum and it is a factor of 2 higher than at the edge of the domain. The calculation has been repeated for several particle sizes. As can be seen in Fig. 3, the dependence on particle size in the spherically symmetric case is weak.

Unfortunately, the azimuthal average does not allow unambiguous separation of all of the physical effects possible in the innermost coma but it does provide more constraints on the problem by giving the dust outflow a quantifiable form (the azimuthal average profile) and is thus extremely useful as a tool.

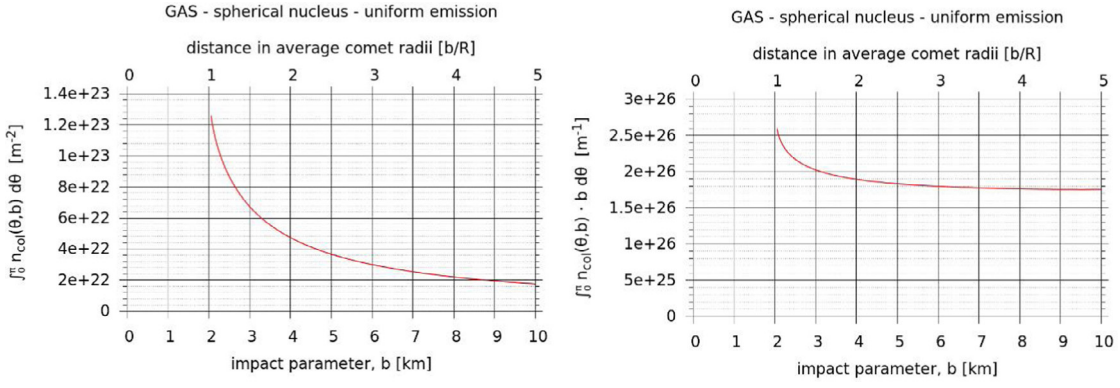

Fig. 2. The integrated dust column density profile (left) shows a direct integrated profile representation of the 2D gas flow field in Fig. 1. The integrated dust column density multiplied by the impact parameter b (right) shows that above the surface (here set at 2 km), the gas column density drops more steeply than 1/r as the gas accelerates into the coma. All points inside 2 km ($b/R = 1$) would be obscured by the nucleus itself.

2.4. Non-radial flow, sublimation, fragmentation and optical depth

Thomas and Keller (1990) showed that a distribution of sources (rather than the isotropic source in Fig. 1), each exhibiting the characteristics of free radial outflow over a finite sized nucleus, would lead to the azimuthal average rising as one approached the nucleus. The possibility of non-radial outflow of dust close to the nucleus was also considered. When viewing the column density (in the form of a radiance) this could not be distinguished from the effects of acceleration without further constraints. Similar behaviour can arise if the particles sublime. After ejection, dust particles will absorb solar radiation and heat up. This can lead to sublimation (Lien, 1990) and hence a reduction in the effective scattering area will ensue which could resemble acceleration. The positive aspect here however is that there is no reason why these effects should operate over the same scale length so that, in an ideal case, these variables might be separated.

On the other hand, for the observations of comet 1P/Halley, the azimuthal average decreased on approaching the nucleus. There are two processes that can lead to such behaviour. Firstly, if dust particles fragment, the effective scattering area increases leading to an increased radiance with distance from the nucleus. On the basis of other observations, this was the preferred mechanism of Thomas and Keller although there is some room for doubt. (It should be noted that fragmentation into less optically active particles would provide the opposite effect and care must be taken to distinguish between the two possibilities. This does however require a substantial number of the particles to be close to the wavelength of the observation.) This was subsequently investigated in more detail by Konno et al. (1989).

The second option was that optical depth effects were becoming increasingly significant above the surface of the nucleus. This influences the proportionality constant, k, in Eq. (3) and could lead to the observed behaviour at 1P/Halley with optical depths of the order of 0.5. If we know the optical depth, τ, at an impact parameter, b_{far}, where optical depth effects are negligible, then the intensity of the scattered flux can be calculated assuming free-radial outflow using the straightforward equation,

$$I(b) = I_0 \frac{b_{far}}{b} e^{-\tau(b_{far}) b_{far}/b}. \tag{8}$$

Given that a straightforward model for particle fragmentation might also be an exponential decay profile (Thomas and Keller, 1990), the two options cannot be separated.

To summarize, the influence on the azimuthal average of the effects considered by Thomas and Keller is illustrated schematically in Fig. 4.

2.5. Gravitationally-bound large particles

One process that was not considered by Thomas and Keller (1990) was the potential effect on the azimuthal average of large numbers of gravitationally influenced particles. In the case of 67P, particles of this type have been frequently touted as major contributors to the dust coma (Fulle et al., 2015) and their effect on the azimuthal average has not yet been assessed although obviously their influence should tend to zero as they leave the Hill sphere at near constant velocity in a nucleus-centric coordinate system.

The existence of significant numbers of large slow moving particles in the vicinity of the nucleus has been established by Rotundi et al. (2015) and Fulle et al. (2015). Evidence of particles falling back to the nucleus (following prediction by Möhlmann (1994) and Crifo et al. (2005)) has been provided by Agarwal et al. (2016) and Lin et al. (2016) and the existence of deposits arising from this process has been provided by Thomas et al. (2015) and Keller et al. (2018). The numbers in bound orbits out to the limit of the Hill sphere have not been determined although estimates for the production rates of large particles have been made (Ott et al., 2017; see also Drolshagen et al., 2017). As has been demonstrated by Richter and Keller (1995), the computation of bound particle orbits in the vicinity of the nucleus and, in the presence of other forces such as gas pressure, is a complex problem. We can however use two simple models to illustrate crudely how gravitationally-bound particles might influence the azimuthal average.

In a first approach we assume that the contribution to the scattering area by gravitationally bound particles is dominated by particles on ballistic (returning) trajectories. In this case we can consider using the Chamberlain model for quasi-collisionless atmospheres (Chamberlain, 1963; Chamberlain and Hunten, 1987) as is common for the simulation of planetary exospheres where collisions between particles are rare. The model describes the density distribution dominated by returning particles as a product of the barometric density and a partition function for the ballistic particles, namely,

$$n(r) = n_0 e^{-(\lambda_0 - \lambda)} \zeta_{bal}(\lambda), \tag{9}$$

with $\lambda(r) \equiv GM\mathcal{M}/(kT_s r)$ the potential energy at distance r, where G is the gravitational constant, $\mathcal{M}$ the mass of the comet nucleus, M the particle mass, k the Boltzmann constant, T_s the effective temperature at the surface, n_0 is the particle density at the surface and $\lambda_0 = \lambda(R)$ the potential energy at the comet surface. Following Chamberlain (1963), the partition function for ballistic particles can be written as

$$\zeta(\lambda) = \frac{2}{\pi^{1/2}} \left[\gamma\left(\frac{3}{2}, \lambda\right) - \frac{\left({\lambda_0}^2 - \lambda^2\right)^{1/2}}{\lambda_0} e^{-\psi} \gamma\left(\frac{3}{2}, \lambda - \psi\right) \right], \tag{10}$$

where $\psi = \lambda^2/(\lambda + \lambda_0)$ and $\gamma(\alpha, x) = \int_0^x y^{\alpha-1} e^{-y} dy$ is the incomplete Γ function. The integral along the line of sight as a function of the impact parameter, b, must be solved numerically. In Fig. 5 we show example calculations with three different values for the gravitational potential energy λ_0 at the surface of a spherical nucleus of 2 km radius. We have multiplied the density integral by the distance to the centre of the nucleus to simulate the azimuthal average and one can see in Fig. 5 the different effect on the product resulting from different values of the gravitational surface potential. The combination of the exponential and the multiplication by b produces a non-linear function which should be evident in the azimuthal average if particles in ballistic orbits dominate the coma of the comet in the first few kilometres above the nucleus surface.

An alternative approach is to determine the azimuthal average under the assumption that the dominant source of scattering comes from particles that are already in bound orbits. Here we can compute Keplerian orbits about the nucleus (as was used for observed individual boulders by Davidsson et al. (2015)) and determine the observed column density dependence. We assume that the orbits are isotropically distributed with apoapsides at the Hill radius and periapsides directly about the surface of a spherical 2 km nucleus. Once again, we are looking for the approximate form of the azimuthal average to be expected by determining the column density. As the orbits are Keplerian in this calculation and the mass of the particles are negligible compared to the mass of the nucleus, there is no particle size dependence. The result of this calculation can be seen as the solid line in Fig. 6. A second calculation has been performed with the periapsis set to 50 km. The peaking in the azimuthal average at this impact parameter is evident.

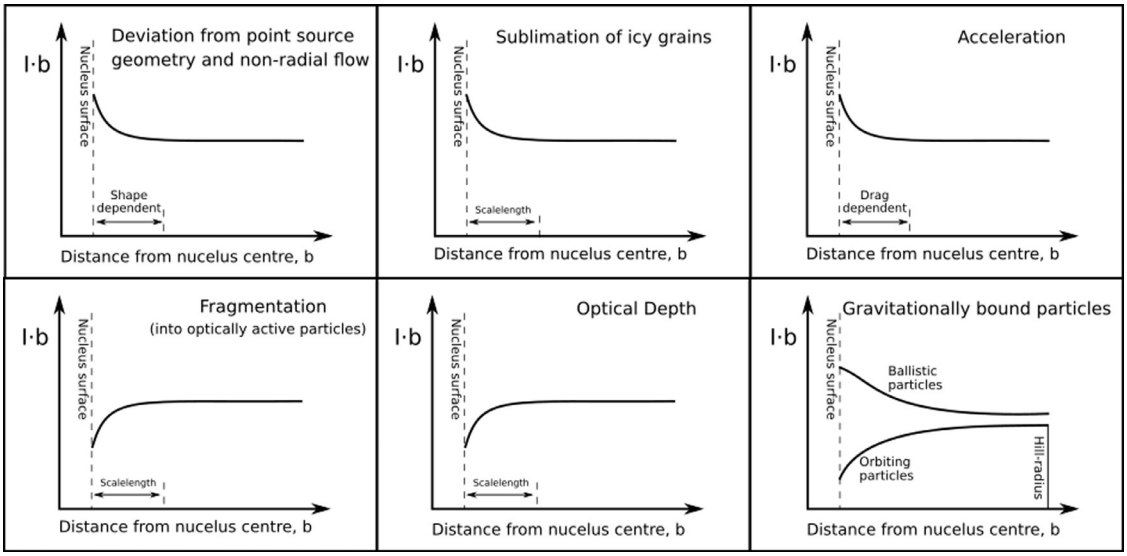

Fig. 4. Schematic diagram of how various near-nucleus processes can affect the azimuthal average. Top left: Deviations from point source geometry and non-radial outflow produce a decrease with increasing distance. Top middle: Sublimation reduces the scattering area but the scale length will be different to that of the non-radial outflow and dependent on particle properties. Top right: Acceleration shows a similar effect but here the scale length is a function of the drag coefficient and the production rate. Bottom left: Rapid fragmentation close to the nucleus increases the effective scattering area so that the azimuthal average rises with distance. The form of the curve is unclear but an exponential function is probably reasonable. Bottom middle: Optical depth effects close to the nucleus mask scattering particles. This reduces with distance as the dust expands, increasing the visible scattering area. Bottom right: Ballistic particles remain close to the nucleus and obviously do not conform to the free-radial outflow approximation. The exact form of the azimuthal average is different for different particle sizes but generally decreases with distance from the nucleus. If particles are in bound closed orbits, the azimuthal average can have several different forms but typically increases with distance from the nucleus out to the Hill radius. The effect of gravitationally-bound particles is discussed more closely in Section 2.5.

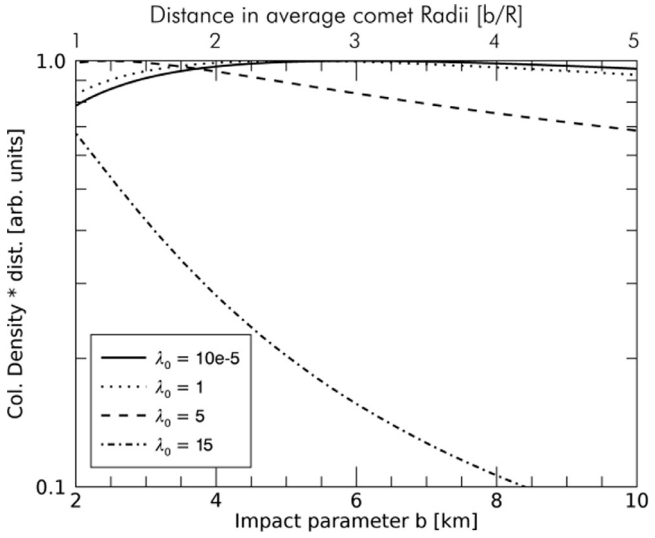

Fig. 5. The product of column density and distance for the Chamberlain model for quasi-collisionless atmospheres dominated by ballistic particles. The maximum with distance of all three curves has been normalised to 1.

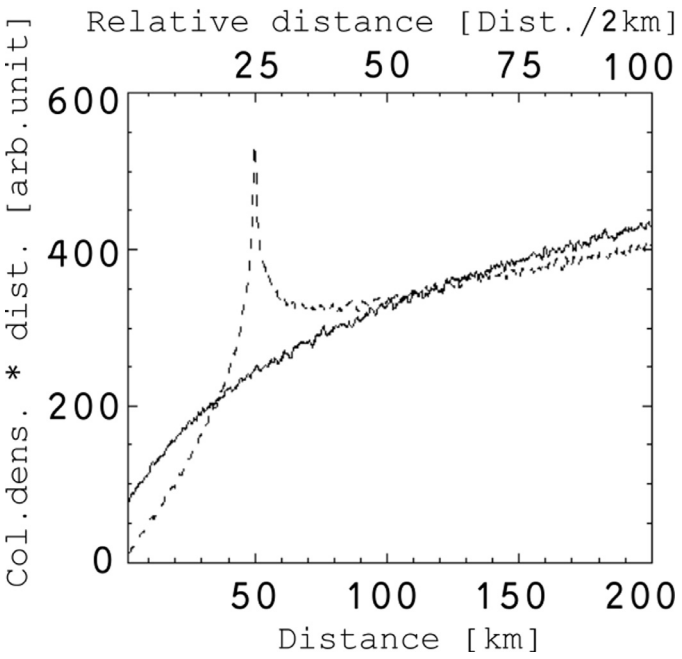

Fig. 6. Simplified calculation of the dependence of the product of column density and distance for gravitationally bound particles within the Hill sphere of 67P. Two different assumptions are shown. The solid line gives the product if the periapsides for the particles are all set to the nucleus radius. The dashed line gives the product if the periapsis for the particles is set to 50 km.

The conclusion from these calculations is that if gravitationally bound particles dominate the scattering area then the azimuthal average will not be constant with distance but will have a curved form. It is conceivable that some combination of the two gravitationally-bound schemes could produce a constant value for the azimuthal average. However, this would need these two schemes to effectively cancel each other out – something which contradicts Ockham's razor. Furthermore, it appears that one might be able to establish an upper limit on the scattering area from slow moving particles if the value of the azimuthal average shows predictable behaviour.

2.6. Observations within the innermost coma

For observations of 1P/Halley and Borrelly, the imaging systems were at large distances from the nucleus when compared to the impact parameters being investigated. For 1P/Halley, for example, impact parameters up to 100 km were observed from 20–

$50{\cdot}10^3$ km. In these cases, the integration of Eq. (1) along the line of sight from $-\infty$ to $+\infty$ is perfectly adequate. For 67P, however, Rosetta was well within the inner coma. For isotropic emission, the finite integral can be calculated. Observing an impact parameter of 10 km from a distance of 100 km from the nucleus, the difference between the finite and the infinite integrals corresponds to ~3%. This observing geometry corresponds to a little less than half the field of view of the OSIRIS WAC and is therefore not negligible. On the other hand, comets do not exhibit isotropic emission. If a cosine distribution for emission is assumed and viewed from the terminator (a typical geometry for the Rosetta spacecraft as will be shown below) then the difference between the finite and the infinite integrals is <0.3% and should be borne in mind through the following discussion.

We now investigate the azimuthal average for 67P.

3. Observations and database construction

3.1. The OSIRIS dataset

The Optical, Spectroscopic, and Infrared Remote Imaging System (OSIRIS, Keller et al., 2007) was the scientific camera system onboard the Rosetta spacecraft. It consisted of two cameras, the narrow angle camera (NAC) and the wide angle camera (WAC). Both cameras were equipped with a series of band-pass filters to study the comet in different wavelength ranges. The 12 NAC filters cover a wavelength range of 250–1000 nm and the 14 WAC filters a range of 240–720 nm.

The two cameras have fields of view of 2.20° × 2.22° (NAC) and 11.35° × 12.11° (WAC) and an angular resolution of 18.6 μrad/px and 101.0 μrad/px, respectively. The images are acquired using 2048 × 2048 pixel backside illuminated CCD detectors with anti-blooming gates, allowing overexposure of the nucleus without leading to saturation artefacts in unsaturated pixels. This is a key property for enabling studies of the fainter cometary dust coma around the bright nucleus.

The entire OSIRIS dataset of comet 67P contains just over 70,000 images taken throughout the mission. The images were acquired in the course of different imaging campaigns dedicated to achieving the scientific objectives although sequences can be used to address more than one objective.

The raw image data from the camera was corrected through a calibration pipeline (Tubiana et al., 2015) and organised into different levels according to the degree of correction. The calibration and correction pipeline includes corrections for analogue-to-digital converter (ADC) offset and gain, bias subtraction, high and low spatial frequency flat fielding, bad pixel and bad column removal, an exposure time normalisation, radiometric calibration and a correction for geometric distortion (resulting in level 3 data, in units of [W m^{-2} sr^{-1} nm^{-1}]). For the analysis presented in this paper, we used images on data correction level 3B, which are additionally transformed from radiometric units [W m^{-2} sr^{-1} nm^{-1}] into dimensionless reflectance units. The reflectance factor is defined as

$$R = \pi \frac{I(i, e, \alpha, \lambda)}{F(\lambda)}, \tag{11}$$

with the observed spectral radiance I, the solar spectral irradiance at heliocentric distance from the comet F, the incidence angle i, the emission angle e, the phase angle α, and the wavelength λ. Note that the solar irradiance was calculated at the central wavelength of each filter.

3.2. Image selection criteria

Since the OSIRIS image campaigns are dedicated to different scientific goals, not all the images are suited to studying dust features in the innermost coma. To select a suitable dataset for analysis, several selection criteria were defined. They were as follows.

- *Data level 3B:* Not all the OSIRIS images were corrected with the full calibration pipeline. We excluded all images from our analysis that were not provided in data level 3B.
- *Full image 2048 × 2048 pixels:* Both OSIRIS cameras use a 2048 × 2048 pixel CCD detector, but not all the images were acquired with the maximum possible field of view (FOV). Since our analysis focusses on dust distribution in the coma, images with the largest FOV are desirable to study changes in the dust outflow from the nucleus as far out as possible.
- *Good coverage of the coma:* In many cases, OSIRIS NAC images showed only the nucleus or only a small fraction of the coma. For the analysis approach with the azimuthal average, it is critical that the coma is visible around the whole nucleus in every direction. We defined the area of interest for dust outflow as the region spanning from the outer limb of the nucleus to about a projected comet centric distance (an impact parameter) of 7 km. Images that do not contain the whole nucleus plus a circular area of surrounding coma including a majority of the defined region of interest were rejected. Because of this constraint, a major part of the images studied have come from the WAC.
- *Field of view of <100 km:* Experience showed that images taken further away and therefore with a large field of view in the target plane did not have sufficient resolution to study the general dust behaviour in the defined region of interest. Therefore, these images with too large a field of view (corresponding to roughly 50 m/px irrespective of the camera used) were excluded from analysis. Most of the images rejected with this fourth criterion date back to the beginning of the mission and were acquired while the spacecraft was first approaching the comet.
- *Lower boundary on coma activity:* In our analysis we saw that an insufficient signal-to-noise ratio leads to meaningless results. Therefore, we excluded images which had a value for the azimuthally averaged dust reflectance at 3 km impact parameter of below $A(b) \sim 1.5{\cdot}10^{-5}$ in reflectance units (corresponding to an azimuthal average of 4.5 cm). This limits our analysis to a time period from February 2015 to November 2015, when the comet showed significant coma activity.
- *Shutter errors:* During certain periods of the mission some problems with the mechanical shutters occurred leading to incorrect exposure of the detector. OSIRIS images acquired with a malfunctioning shutter were not a priori excluded from the database, but could be identified and were excluded from analysis. Some recovery of these data might be possible in some cases at a later date.
- *Ghosts:* On some images, artificial features are seen superimposed on the dust coma. These are so called ghosts arising from internal reflections from optical components of the system. The ghosts are always located in the same place if they appear in an image, but they are in general not very prominent. Nevertheless, the ghost blends with the dust coma around the nucleus and influences our dust analysis. At the moment, we do not apply any corrections for the effects of the ghosts. We assume that the images with a ghost present do not significantly influence the statistical results of our analysis. Although, they might represent a source of systematic error if the coma is faint. To reduce the influence of ghosts in our analysis as presented in this paper we excluded images acquired with the UV and IR filters, since these images are more prone to show ghosts than for example images acquired with band-pass filters in the visible range.

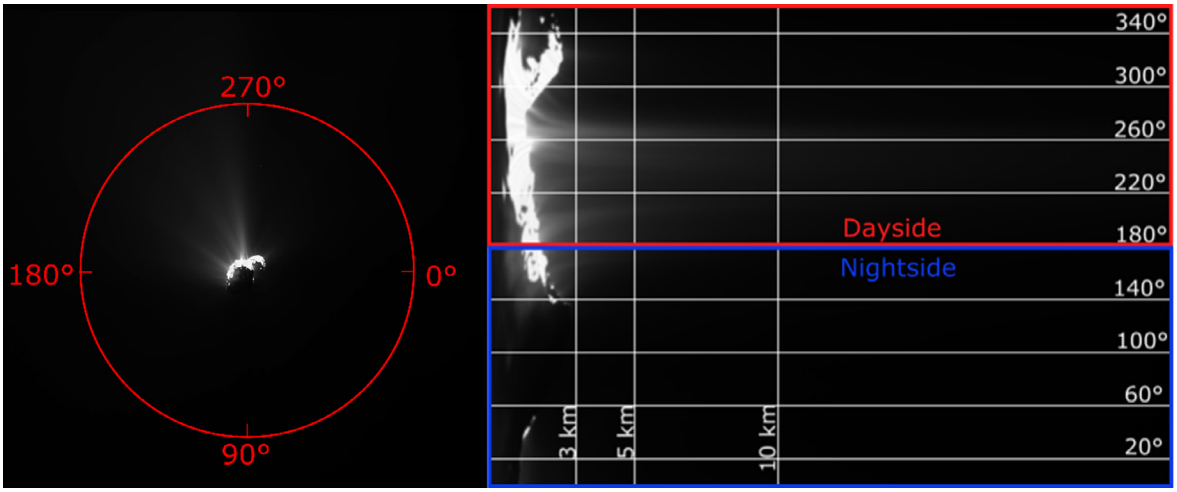

Fig. 7. Left: The original OSIRIS WAC image was taken pre-perihelion on the 05.08.2015 with filter combination 18 and a phase angle of 89.5°. An over-plotted angle specification shows the allocation of the transformation angle for the polar transformation. Right: Polar coordinate transform. Impact parameter is along the x-axis and the azimuth angle along the *y*-axis. The nightside is defined as the region inside transformation angle 0°−180° and dayside as 180°−360°, because the sun azimuth angle in this image is exactly 270°.

- *Gas emission contribution in OI-filter*: In another step we excluded images acquired with the WAC narrowband filter combination 17 (OI-filter at 630 nm). Comparisons of intensity profiles of images taken with the same observation geometry but with different filters indicate that in F17 images a significant amount of the intensity signal comes from gas emission contributions. Although Bodewits et al. (2016) suggested that there is gas contamination in the F18 (OI continuum filter at 610 nm), the azimuthal average plots in that filter and in the F16 (Na filter at 589 nm) show similar behaviour which only deviates in the order of the image error. Hence, the F17 images were excluded in our dust coma analysis to prevent bias from gas contribution. We return to this issue below.

This selection left us with a total of 3553 images in the dataset for analysis, thereof 1880 WAC images and 1673 NAC images.

3.3. Single image analysis

To generate the data included in the database, every suitable image was passed through an automated image analysis sequence. In this paragraph, we explain with an example image (Fig. 7) how the image analysis was carried out.

- Transformation into polar coordinates: In a first step, the original OSIRIS image was transformed into polar coordinates (Fig. 7).
- The origin was set to the image coordinates of the nucleus centre of mass, which were determined using the SPICE library and appropriate kernels. The same origin was also used for the calculation of our impact parameter b ($b = 0$ at the image coordinates of the nucleus centre of mass).
  In the polar transformed image, two regions were defined: the dayside and the nightside. Both regions are defined taking into account the projected direction to the sun in the image plane. The dayside includes the regions defined as the solar azimuth angle $\pm 90°$ and the nightside includes the regions corresponding to the complementary 180° in transformation angle. It is important to keep in mind that the definitions for day- and nightside as introduced here do not follow the terminator definition for the illuminated dayside and non-illuminated nightside except in the case when the phase angle takes a value of exactly 90°. But since about 50% of the images in the dataset were taken with a phase angle between 80°−100°, the nomenclature is reasonably accurate. This division of the full angle into two regions was intended to gain a better understanding of the dust outflow. As will be seen, this does indeed provide some additional insight.
- *Average azimuthal dust reflectance ($A/2\pi$):* In a second step, dust profiles of azimuthally averaged dust reflectance values with increasing impact parameter were generated (Fig. 8 left). The average dust reflectance value as a function of the impact parameter was computed by taking the mean value of all pixel intensities along every column of the polar transformed image matrix. This is equivalent to an azimuthal integration of dust reflectance along a circular path around the comet nucleus over a full angle at different impact parameters (divided by 2π radians). The analysis was carried out for three different integration ranges: the full azimuthal angle (FA, 0°−360°), the dayside (DS, 180°−360°), and the nightside (NS, 0°−180°). The limb of the nucleus is located between 2.5 and 3 km from the origin depending on the orientation of the nucleus in the image.
  In our example image, the value of $A/2\pi$ shows a smooth decline starting at radial distances larger than about 3 km. This corresponds to the part of the image where the measured reflectance comes from the light scattered by dust in the coma close to the nucleus surface. We observe this behaviour for all the analysed images.
  Naturally, the average dust reflectance on the dayside is higher than the average dust reflectance over the full angle. The average dust reflectance on the nightside is consequently lower.

- *Azimuthal average multiplied by the impact parameter:* To study the nature of the decline in reflectivity more closely, the $A/2\pi$ values were multiplied by the impact parameter, b, to give $\bar{A}$. The profile of the azimuthally integrated dust reflectance multiplied by the impact parameter will be referred to as the "$\bar{A}$-curve" in this paper.

In our example (see Fig. 8 right), we observe a distinct decrease of the $\bar{A}$-curves close to the nucleus (impact parameters between 3 and 5 km) until the curve reaches a linear, roughly constant, behaviour at impact parameters between 9 and 11 km from the nucleus centre. The observed form of the $\bar{A}$-curves in our example image (steep decrease of the $\bar{A}$-curve close to the nucleus and transition towards constant behaviour around an im-

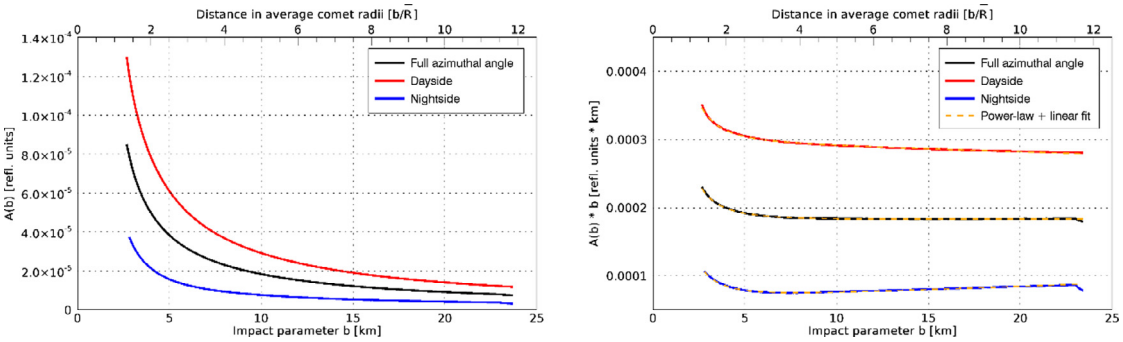

Fig. 8. Left: Average azimuthal dust reflectance with increasing impact parameter of the example image. The different colours correspond to different integration ranges: full azimuthal angle (0°–360°), dayside (180°–360°) and nightside (0°–180°). Right: Average azimuthal dust reflectance multiplied by the impact parameter b (Ā-curves).

Table 1
The slope parameters w and the parameter errors from the fit in units of %/km. And the starting point of linear behaviour of the Ā –curve for the full angle, the dayside and the nightside.

	Linear gradient w	Gradient error σ'_w	Starting point
Full angle (FA)	0.05%/km	0.02%/km	9.7 km
Dayside (DS)	−0.21%/km	0.01%/km	10.8 km
Nightside (NS)	0.98%/km	0.03%/km	10.5 km

pact parameter of ∼10 km) represent the typical Ā-curve behaviour which we observed in our analysis. We identified two different behaviour regimes in the profile curve: the decrease of azimuthal average with distance close to the nucleus, which we will refer to as the "acceleration region" (although acceleration may only be partially responsible for the observed effects), and the "linear regime" at larger impact parameters. A constant behaviour in the linear regime of the Ā-curve would correspond to a 1/b-behaviour of dust outflow in the respective region, which is expected for free-radial outflow in the absence of phenomena modifying the total dust particle scattering cross-section. (This is the expected "1/r law".) In the example analysis, the Ā-curve for the full azimuthal angle shows a nearly constant behaviour, while the curve for the dayside is slightly decreasing. On the nightside we observe a slightly increasing slope. A quantitative analysis of the curve gradients is given in Table 1. The noticeable drop at the end of the Ā-curve in Fig. 8 (right) is an artefact from image transformation and has no physical meaning.

To quantify the linear gradients of the Ā-curves, we fitted the curve with a function of the form

$$f(b; u, v, w, z) = \frac{u}{b^v} + wb + z, \tag{12}$$

where b is the impact parameter, u and v are constants describing the decrease in $\bar{A}$ close to the nucleus, and w and z are constants that determine the behaviour of $\bar{A}$ in the linear regime of the curve. The slope parameter w determines the slope of the linear regime of the Ā-curve and z is a constant that is related to the value of $Af\rho$ in units of [reflectance units · km]. Note that the actual functional form is unknown although we do not rule out the possibility that the constants u and v might eventually be inverted in some way to provide physical insight into the processes close to the nucleus. To fit our data curves, we used the least-squares routine MPFIT based on the Levenberg–Marquardt algorithm implemented by Markwardt (2009).

For theoretical force-free radial dust outflow we would expect the linear slope parameter w to be exactly 0 from the point source outwards. In the real case with a finite nucleus and acceleration we still expect w to be 0 but to reach this value at a distance from the nucleus defined by the gas drag, gravity and the nucleus shape. A significantly increasing ($w > 0$) or decreasing ($w < 0$) Ā-curve would indicate deviations from free-radial outflow behaviour, leaving room for other driving mechanisms at work in the innermost coma (e.g. fragmentation or gravitationally bound particles). It should be clear that our null hypothesis is that including gas drag, gravity and the size of the finite source alone is sufficient to model the observations.

The errors on the fit parameters were calculated during the fitting process taking into account the errors on the azimuthal average, which were estimated with the help of the background standard deviation in a 10 × 10 pixel frame on the calibrated image. A statistical analysis of the general behaviour of the dust profiles is presented below.

With the help of the fit to the Ā-curve it is possible to determine the starting point of the linear behaviour. We define the starting point, b_{start}, as the impact parameter where the ratio of the linear contribution to the total fit function value exceeds 99%, which means the contributions from the power-law has dropped below 1%, i.e.

$$b_{start} \text{ where } \frac{wb + z}{\frac{u}{b^v} + wb + z} = 0.99$$

For our example image, the values for w, the errors in w and the starting points for linear behaviour of the Ā-curve for full angle, dayside and nightside, respectively, are given in Table 1. The linear gradient is specified in units of [%/km], which allows a more intuitive feeling of the significance of the slope. For that we normalise the gradient from the fit with the averaged value of $\bar{A}$ over the last two kilometres in the profile and multiply by 100. The errors provide an assessment of the significance of the result.

3.4. The Osimana database

The main purpose of the Osiris Image Analysis (Osimana) database is to collect the data from the single image analysis of the whole dataset. The following parameters were produced.

Average azimuthal dust reflectance: From the averaged azimuthal dust reflectance profile over the full angle four values at different impact parameters (b = 3 km, 5 km, 10 km and b_{max}) were saved. The maximum impact parameter b_{max} is different for each image and depends on the field of view and the position of the comet in the image and is included in the database.

Fit parameters: The results from the fits to the Ā–curves were saved in the form of the four fit parameters and the corresponding parameter errors for the full angle, the dayside and the nightside analysis.

Other image information: In addition to the data from image analysis, the database contains selected image information extracted from the image header or calculated with the help of the SPICE kernels such as comet-centric distance of the spacecraft or the phase angle of the observation.

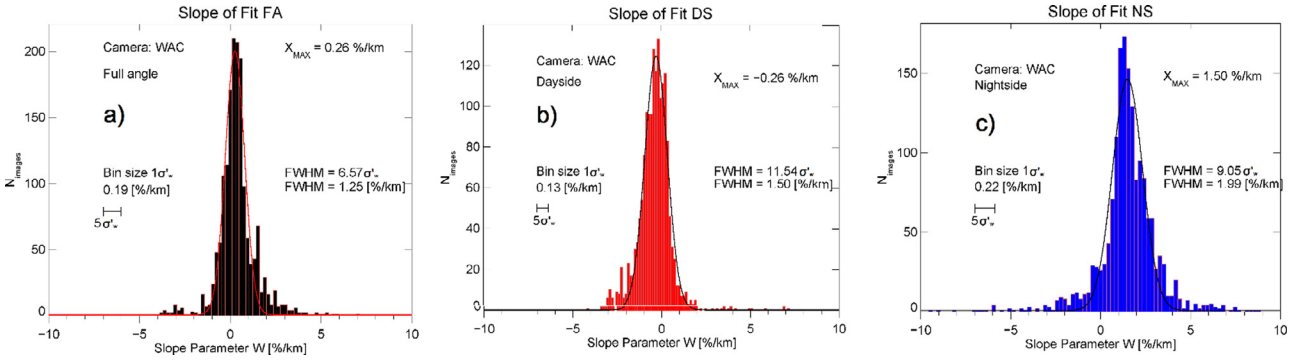

Fig. 9. Histograms of linear gradients in units of [%/km] from analysis of data from the WAC camera. (a) This diagram shows the analysis for the dust integration over the full angle, in (b) we see the same histogram for the analysis on the dayside and in (c) for the nightside. Positive gradients correspond to an increase in the original Ā-curve, negative gradients to a decrease. A linear gradient of zero indicates a constant behaviour of the Ā-curve, which directly relates to a 1/r-behaviour for the dust outflow.

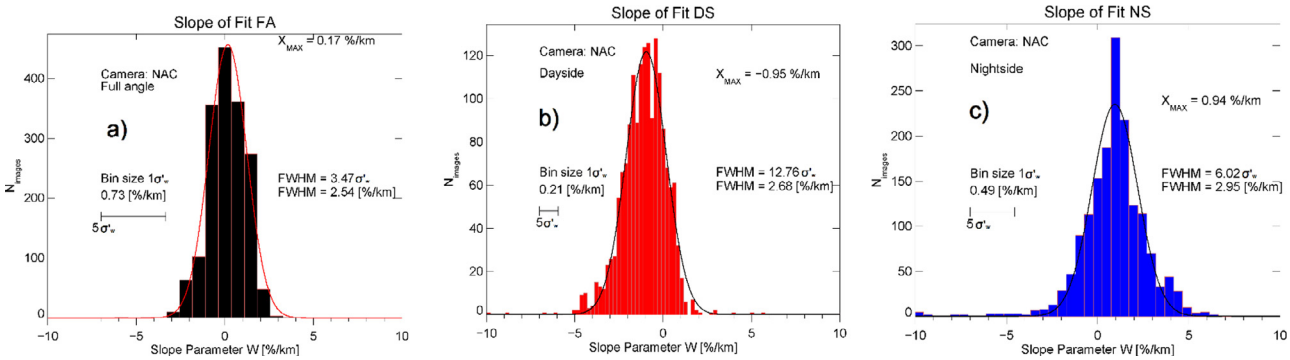

Fig. 10. As Fig. 9 but for the NAC images in the database.

All in all, the database contains a huge amount of information for the study of the dust dynamics in the innermost coma and we expect a significant amount of output from detailed analysis. The major potential of the database lies in statistical analysis of different properties of the dust coma and their evolution over a longer period of time. Here, we provide an initial overview of some of the key properties.

4. Analysis

4.1. Approach to "1/r" behaviour

As illustrated in Section 2, in the absence of effects from gravitationally-influenced particles and effects influencing the total particle scattering cross-section (e.g. fragmentation), we expect the azimuthal average to approach a "1/r law" as the impact parameter increases and thus the linear slope, w, should be zero for the azimuthal average, $\bar{A}$.

We have plotted histograms showing the distribution of the fit parameter w, which corresponds to the slope in the linear regime of the Ā–curve. The histograms in Fig. 9 are for the WAC dataset while Fig. 10 shows the analysis for the NAC. The bin size in each histogram was chosen to be the median value of the uncertainties of the corresponding slope parameters w in [%/km], σ'_w.

In Fig. 9a), the complete azimuthal average is shown. A comparison with a Gaussian distribution shows that the derived values of w closely follow a normal distribution about the mean. The distribution of slope parameter w peaks at 0.26%/km, about 1.5 σ'_w from the expected value of zero. There is a small tail towards values of $w > 0$ indicating an occasional tendency for $\bar{A}$ in some images to decrease less steeply than 1/r.

If the angular integration is confined to the dayside only, the value of w is significantly lower. The distribution has its maximum at a value of −0.26%/km. We therefore observe a tendency for falling curves on the dayside as our example image analysis in Section 3 already suggested. If the angular integration is confined to the nightside, w is higher. In most of the images we observe rising Ā-curves on the nightside and the mean value of the distribution is at about 1.5%/km. This means that the dust brightness with impact parameter is in general decreasing less steeply than 1/r on the nightside. The error analysis indicates that this result is significant.

The width of the distribution of the full angle analysis is quite broad with a half width at half maximum being more than 6 σ'_w where the sigma value is derived from the median of the error in w in the least-squares fit. Changes of this magnitude are not negligible as they would, if significant, correspond to changes in the effective scattering cross-section of the particles over a distance of about 10 km. On the other hand, more than one physical process would need to be at work to produce both negative and positive values of w. To illustrate the difficulty, the dust would have to be subliming some of the time and fragmenting into optically active daughters at other times. This is conceivable but seems rather improbable. This may indicate that our error analysis has been slightly over-optimistic.

The NAC results show very similar trends although the values for the peaks of the histograms are slightly shifted towards lower w compared to the WAC analysis but are identical within error. For the full azimuthal average, the peak of the Gaussian fit to the distribution is closer than 1 σ'_w to a value of zero (Fig. 10a). For the dayside analysis, we see that the distribution shows a peak at about −1%/km. The distribution for the nightside analysis shows the same shift towards lower linear gradients, although its mean value remains positive at 0.94%/km.

The agreement between the broad-band filters used in the NAC and the narrower band filters used in the WAC for the full angle

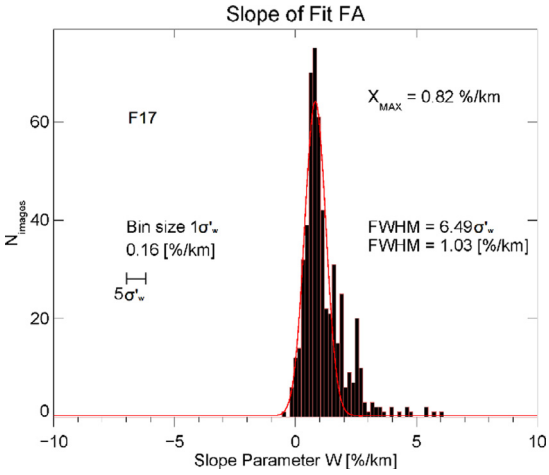

Fig. 11. Distribution of the slope parameter, *w*, for images acquired in filter 17 (OI) showing a deviation from 1/r at the 5 sigma level.

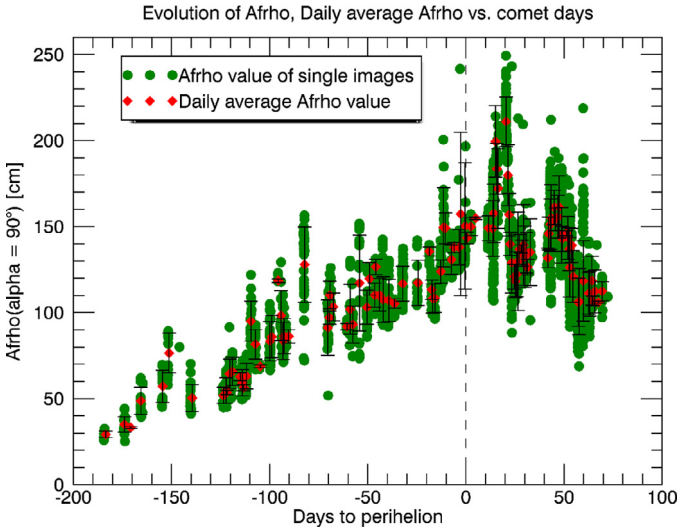

Fig. 12. The resulting Afρ values calculated from the constant value, *z*, from the fit to the azimuthal average with impact parameter, *b*. The variation with heliocentric distance is to be expected. A phase angle normalization to $\alpha = 90°$ has been applied to the data shown in this plot. The green data points mark Afρ values calculated for single images and the red data points indicate averaged Afρ values over one comet day. (For interpretation of the references to colour in this figure legend, the reader is referred to the web version of this article.)

indicates that gas emissions are not of significance (within the error of the measurement) for this analysis.

There are potential explanations for the observed effects. The difference between the dayside and the nightside slopes are possibly the result of transport of dust from the dayside to the nightside hemisphere, leading to decreasing slopes on the dayside and increasing slopes on the nightside. This would have a larger relative effect on the nightside given that the nightside is far less active than the dayside. We shall show in the next section that this is a plausible explanation. An alternative is that the shadowing of the dust in the nightside coma by the nucleus itself has a measureable effect. The nightside hemisphere subtends 2π steradian while the shadowed solid angle is a function of the impact parameter. If nightside dust emission were isotropic this could produce an effect equivalent to +1.2%/km in the behaviour of $\bar{A}$ and thus smaller than the observed mean value. Additionally, the dust is certainly not isotropic and we would assume this to be a stringent upper limit. In conclusion, the shadowing from the nucleus cannot explain the whole amount of rising nightside curves, although it is probably responsible for a part of the effect.

It might be thought that radiation pressure effects producing reflected particles might contribute to the brightness in the nightside coma. However, it is fairly simple to demonstrate that this effect so close to the nucleus is probably negligible.

The differences in the peaks of the distributions between NAC and WAC illustrates a small inconsistency. The calibration of the two cameras seems an improbable explanation. However, it is to be noted that, for the NAC images, the field of view is generally smaller than for the WAC. Therefore, we are probably biased by images where the decrease of the Ā-curve in the acceleration region still dominates the general behaviour and where there are insufficient data points in the linear regime to guide the solution. This is also apparent from the error on the linear slope parameter which is systematically higher for the NAC. The phase angle distribution (for the NAC most images were at phase angles below 90°) may also play a role.

Based on our statistical analysis of the linear gradients we conclude that the dust outflow in general converges towards a 1/r behaviour in the inner coma. Although the statistical analysis provides a clear picture, the rather broad distributions leave some room for further investigation of individual images to establish why some images deviate from the mean.

We also note in passing that the azimuthal average in the OI (630 nm) filter deviated from zero by more than 5 σ'_w indicating gas contamination in this filter (Fig. 11). Further detailed comparison is a subject of future work.

4.2. A rough estimate on the influence of gravitationally bound particles

Given the major discussion on-going about the relative number of large non-escaping particles in the emitted flux, we have used the calculation in Section 2.2 to make a crude estimate. Non-escaping particles are not force-free and do not follow a 1/r law as shown in Section 2.2. Assuming a λ_0 of 5 at the surface of the nucleus in the Chamberlain model, the brightness decrease with distance falls corresponding to $w < -3$%/km over impact parameters comparable to those used in our data analysis. The histograms are showing values of > -1%/km. Thus, if a $\lambda_0 = 5$ is realistic, the proportional scattering area of particles in these ballistic trajectories must $< (1/3)$ or < 33%. Clearly, the uncertainty on the initial ejection velocity of these particles would make this estimate highly uncertain. For lower values of λ_0 at the surface, the effect would be difficult if not impossible to extract from the profile cuves in our approach. However, depending on the value of λ it indicates that the tendency towards 1/r shown by our analysis may place a rigorous constraint on the numbers of returning particles. This will be the subject of further work.

4.3. The value of the constant, z

The fitting routine provides, as output, the constant, *z*, which is the value that $\bar{A}$ approaches at large distances from the nucleus assuming free radial outflow. *z* is a value that can directly be linked to the Afρ value introduced by A'Hearn et al. (1984), which enables direct comparison of coma activity of comets.

In Fig. 12, we see Afρ expressed as a function of time to perihelion and therefore heliocentric distance. The plot shows how the Afρ value was increasing as the comet moved towards perihelion and became more active.

To calculate Afρ for our observational data we used the fit offset parameter *z*. In a first step, *z* was normalised to a uniform

phase angle of 90°. This was achieved with the help of the scattering phase function of 67P as derived from OSIRIS observations by Bertini et al. (2017). Because no analytical description of the phase curve was available we used a simple polynomial fit of 6th order to Bertini's data, which describes very well the phase function in the pivotal range between 20° and 150° and is sufficiently accurate for our purposes.

The relationship of the phase angle corrected offset parameter, z, to Afρ is not completely straightforward. Fink and Rubin (2012) use the equation

$$F_{obs} = \int \frac{2\pi Ib}{\Delta^2} db$$

for the flux from a comet when using a circular aperture centred on the comet nucleus that is equivalent to a projected radius b at an observer-comet distance of Δ. Multiplying the observed radiance, I, by $\pi/F_\odot$ allows us to replace the flux with the reflectance so that

$$\pi \frac{F_{obs}}{F_\odot} = \int \frac{2\pi Rb}{\Delta^2} db.$$

Eliminating the π, we have an expression for $F_{obs}/F_\odot$ which can be substituted in A'Hearn et al.'s definition of Af, i.e.

$$Af = \frac{4\Delta^2}{b^2} \frac{F_{obs}}{F_\odot}$$

which gives

$$Af = \frac{8}{b^2} \int Rb\ db.$$

For the force-free radial outflow case, Rb is a constant and its mean value on a circular path centred on the nucleus is our $\bar{A}$, or in this case the value of our constant offset parameter z. This shows that

$$Af\rho = 8\bar{A} = 8z$$

The results shown in Fig. 12 indicate that our maximum value of Afρ is about 210 cm occurring 20 days after perihelion. This is in remarkable agreement with Afρ values given by Agarwal et al. (2007) in the pre-prime mission dust environment model for 67P. Snodgrass et al. (2016) measured 400 cm at a phase angle of 34° (Snodgrass, pers. comm.). They then extrapolated this to zero phase angle to get 1000 cm. We have normalized them at 90° using Bertini et al.'s phase curve. One should note that 90° is almost a minimum of the phase curve and is very appropriate for normalization of OSIRIS observations. Hence, there is actually consistency – at least in the trend – with the Snodgrass et al. result because at 90° their Afρ leads to a value that must be <400 cm.

In our data analysis we see significant diurnal variations in the observed Afρ values. In Fig. 13, an example of the observed variations is given. The data were acquired between 04–05.05.2015. The data points follow a periodic curve with two maxima, one with a large amplitude and one with a smaller amplitude. The variation is around 30% peak-to-peak. We observe a periodicity of roughly 0.5 Earth day which corresponds to the spin period of 67P of ~12.4 h. The diurnal variations are thus most probably an effect of the irregular shape and an inhomogeneous surface activity of comet 67P.

4.4. Derivation of the starting point of linear behaviour

The fitting routine can also provide an estimate of the distance from the nucleus at which 1/r behaviour can be assumed. We referred to this above as the "starting point". We determined starting points for every image in the analysis (Fig. 14). Because we observe significant changes in the starting point due to different viewing geometries, the major contribution being a periodic change arising from comet rotation, we calculated the average starting point

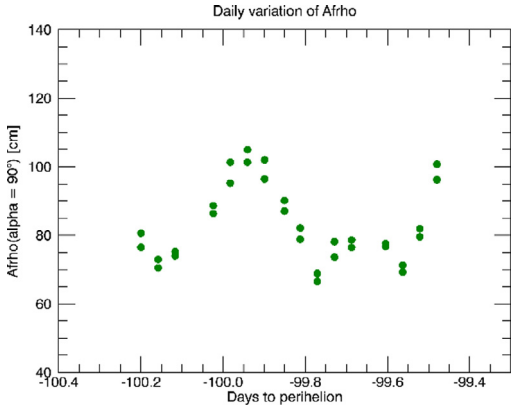

Fig. 13. Diurnal variations of Afρ value. The data points were acquired between the 04.05.2015 and the 05.05.2015 with the WAC camera and filter combination 18. The variations are most probably an effect of the complex shape and the inhomogeneous activity of comet 67P.

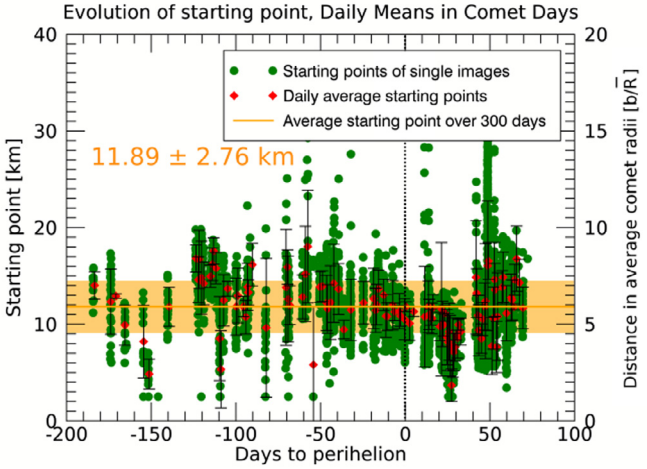

Fig. 14. This diagram shows the starting points of the linear behaviour of the single image analysis in green dots. The average starting point over one comet day is plotted in red diamonds. The errors on the average starting points arise from statistical standard deviations of the daily changes. In orange the mean starting point over the whole time period is plotted. (For interpretation of the references to colour in this figure legend, the reader is referred to the web version of this article.)

for each comet day as the mean value of the starting points of all single images acquired at that same day. The error on the average starting point is merely the standard deviation of the single starting points. The mean value of the starting point over the period of time covered by our dataset was then found to be 11.9 ± 2.8 km. Thus, in the general case, effects influencing deviations from 1/r close to the nucleus are becoming insignificant at distances larger than about 6 comet radii from the nucleus centre. However, from the plot we can see that the starting point is probably not constant with time. A minimum is seen close to perihelion near the peak of production rate.

5. Modelling of the dust outflow and comparisons

5.1. The DSMC approach

In the introduction, we have already shown an example of a DSMC gas dynamics simulation for a spherically symmetric case to illustrate the effect of acceleration on the azimuthal average in a simplified model and to show that we can deduce profiles from our simulations that can be compared to results from data analysis. The code used is called UltraSPARTS (http://www.plasmati.tw) and

is a commercialized derivative of the PDSC++ code (Su, 2013) used in previous papers (e.g. Marschall et al., 2016, 2018). PDSC++ is a C++ based, parallel DSMC code which is capable of simulating 2D, 2D-axisymmetric, and 3D flow fields. The code has been developed over the past 15 years (Wu and Lian, 2003; Wu et al., 2004; Wu and Tseng, 2005) and contains several important features including the implementation of 2D and 3D hybrid unstructured grids, a transient adaptive sub-cell method (TAS) for denser flows, and a variable time-step scheme (VTS). In the parallel version, computational tasks are distributed using the Message Passing Interface (MPI) protocol. A Domain Re-Decomposition (DRD) method, to optimize the parallel performance, has also been implemented (Liao, 2017).

In addition to spherical cases, the 3D shape model of the nucleus can be integrated as the input surface into the computation with the help of a grid generation program. Here, we use the GRIDGEN program from Pointwise to map the SHAP7 shape model (Preusker et al., 2018) of the nucleus of 67P into the simulation code.

To calculate the surface gas flux used for the boundary condition in our numerical simulation we impose a simple thermal model neglecting thermal conductivity (Gulkis et al. (2015); Schloerb et al., 2015) but including sublimation of water ice. The resulting gas production rate is thus driven only by the incidence heat flux from the solar radiation and we therefore call this type of boundary condition purely-insolation driven outgassing. A more thorough description of the simulation setup and an extensive parameter study including comparisons of the model results with Rosetta OSIRIS and ROSINA (Rosetta Orbiter Spectrometer for Ion and Neutral Analysis) data is presented in Marschall et al. (2016).

Once the gas flow field has been derived, the motion of dust particles within the flow is calculated using equations of motion based on drag and gravitational forces as has already been shown for the spherical case in Section 2. The complex shape of the comet has been taken into account in the gravitational model. The model assumes a total nucleus mass of 1×10^{13} kg (Sierks et al., 2015). For the dust particles a constant density of 440 kg/m^3 was assumed. A more detailed description of the used gravitational models is also presented in Marschall et al. (2016).

The intention of this section of the paper is to demonstrate the validity of the use of the azimuthal average and to illustrate that a numerical model of the dust outflow successfully reproduces most of the features seen in the analysis of the data presented in Section 4. We will not stress and/or optimize the boundary conditions of our simulation in detail (as has been done in Marschall et al. 2016). The aim is to illustrate the deviations from 1/r resulting from breaking point source or spherically symmetric geometry using a realistic shape model and a realistic activity distribution. We begin however by returning briefly to the spherical case.

5.2. Simplified cases – azimuthal average

We applied our method of image analysis to simulation results generated from numerical model calculations of gas and dust flow and analysed profiles calculated as the integral of the column density multiplied by the impact parameter around the full azimuthal angle on concentric circles from the comet centre. The latter corresponds directly to the azimuthal average. The gas calculations have been carried out for an insolation driven case with no thermal inertia implying peak emission from the sub-solar point and the emission decreasing to zero at the terminator. The viewing geometry in all four cases in Fig. 15 correspond to 90° phase angle observations. In Fig. 15(a), (c) and (d) the spherical model was used in the simulation and only in case (b) the shape model of 67P was used. In this section we use the model calculations to demonstrate the dependency of the behaviour of the azimuthal average in the acceleration region on particle size and production rate. As will be seen, this shows the challenges we are facing when studying the acceleration region in remote sensing data.

The profiles in Fig. 15(a) were generated with a gas production rate of $Q_g = 2$ kg s^{-1} and the dust calculations on the gas flow field were performed for five different particle sizes between 0.01 and 1000 µm. We observe a dependency of the behaviour of the "acceleration region" in the profile curves on the different particle sizes. The azimuthal average of simulation results calculated with larger particles shows a tendency to decrease less steeply close to the comet surface.

In Fig. 15(b) we used the same model specifications but instead of the spherical nucleus the shape model of 67P was used as the input boundary of the simulation. The profile curves show the same fundamental behaviour seen in Fig. 15(a). Because of the complex shape of the nucleus of 67P, the azimuthal average cannot be evaluated down to the surface and a large part of the "acceleration region" is lost for analysis.

In both cases, the differences between the profile curves of different particle sizes are rather small. The slightly less steep decrease in the "acceleration region" for large particles could be an effect of gravity which is trapping particles in ballistic trajectories close to the comet and thus causing the dust brightness to decrease less steeply. However, the differences are so small one could probably not distinguish between the different particle sizes only from the behaviour of the azimuthal average in data analysis from OSIRIS images.

In Fig. 15(c) we show the dependency of the behaviour of the azimuthal average in the acceleration region on changes in the gas production rate. Three simulations with three different gas production rates were analysed for a particle size of 90 µm. The high production rates (20 and 200 kg s^{-1}) show very similar behaviour and decrease more steeply in the "acceleration region" than the low production rate (2 kg s^{-1}) case.

In Fig. 15(d) a comparison of profile curves shows that we conserve the behaviour of the dust outflow if production rates and particle sizes are scaled proportionally. This can easily be seen from the drag equation. The behaviour holds for particles large enough such that their speed is much smaller than the gas speed but not as large such that their dynamics is influenced significantly by gravity. Any size distribution dominated by this intermediate size range will thus also scale in the mentioned manner. This also indicates that we cannot determine production rate or particle size from the behaviour of the azimuthal average alone because there are several different combinations leading to exactly the same behaviour. On the other hand, this gives us the opportunity to compare low production rate simulation cases with image analysis from images acquired during perihelion transit by simply taking into account that the results apply to different particle sizes that scale proportionally to the production rate.

5.3. Simplified cases – dayside–nightside transport

In the analysis of the linear slope parameter w in Section 4.1 we saw a strong indication for lateral dust transfer in form of a significant asymmetry in the results for dayside and nightside. By studying this phenomenon in numerical simulations with different setups, we show that the irregular shape of the nucleus of 67P has an important influence on the rate of dust transfer towards the nightside.

In Fig. 16 (left) we can see a calculation for a spherical nucleus of 2 km in radius. The gas solution is again an insolation-driven case with no thermal inertia. The dust solution has been calculated for 10 µm particles only for simplicity. The azimuthal average has been computed for the full 2π about the nucleus. The day-

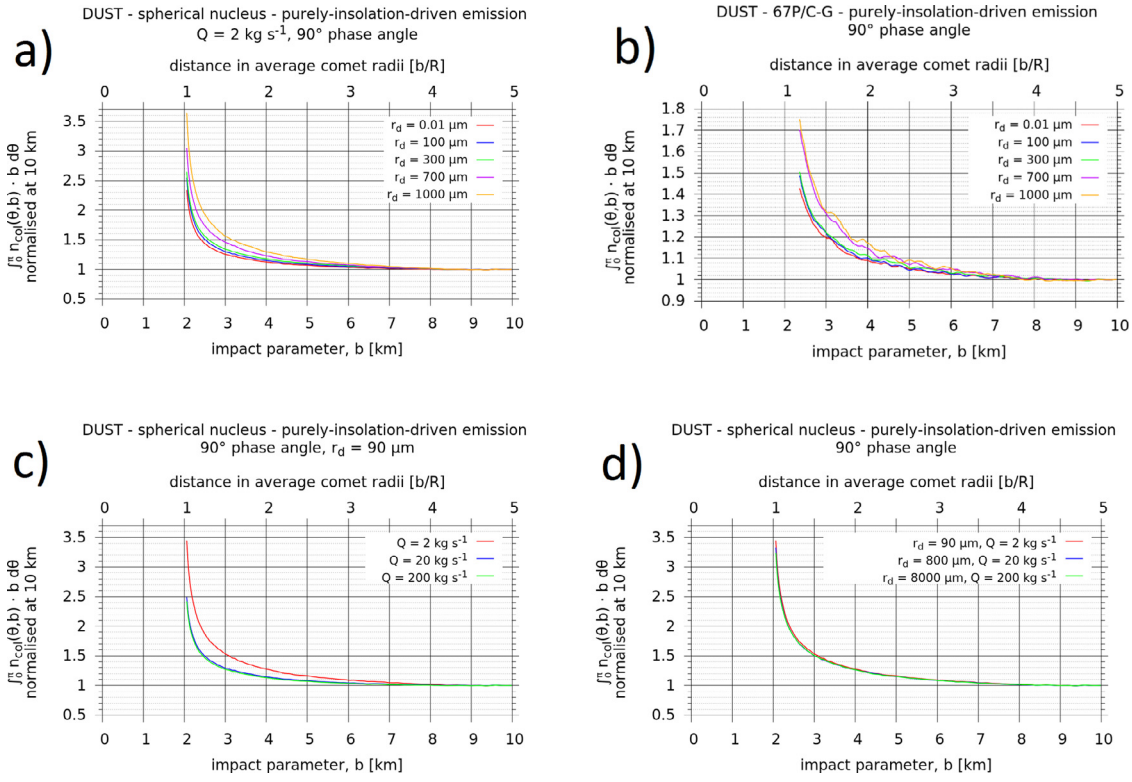

Fig. 15. The different plots show profiles of column densities multiplied with impact parameter, which is proportional to the azimuthal average, $\bar{A}$, of simulation results. The model uses a sphere with radius 2 km as an input boundary, except in plot (b) for which the shape of 67P was used. The model includes only acceleration of gas and dust and gravity from the nucleus. Some model specifications are given in the plot legends. The plots in panels (a) and (c) clearly show that the dust outflow behaviour in the acceleration region is dependent on both, the particle size and the gas production rate. A comparison with panel (b) shows that the dust outflow behaviour shows similar results for simulations based on the 67P shape model. The plot in panel (d) illustrates that different combinations of particle size and production rate lead to exactly the same behaviour in dust outflow and are thus indistinguishable.

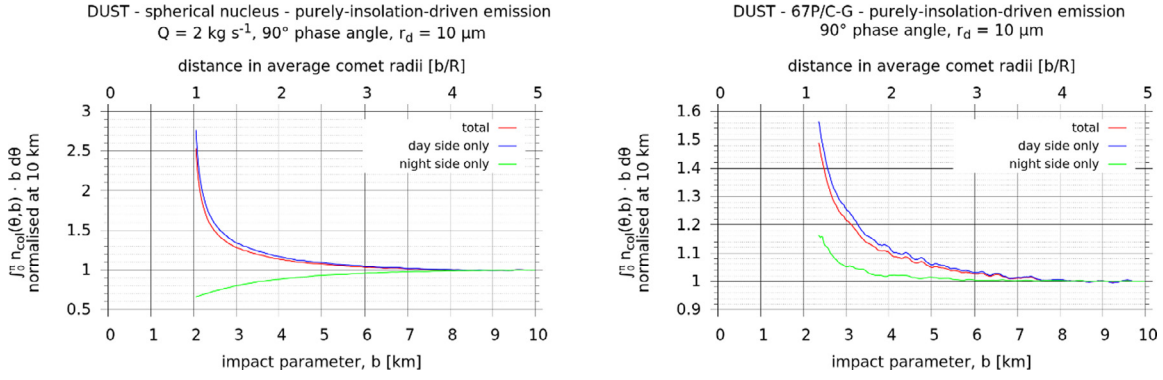

Fig. 16. The azimuthal average for model calculations. Left: For a spherical nucleus. Right: For a 67P shape model. The two calculations have been made for identical conditions. A gas production rate of 2 kg /s has been used. 10 µm particles have been used and the azimuthal average has been computed at a phase angle of 90°. Plots integrating over the dayside and the nightside separately are shown. The plots have all been normalised at an impact parameter of 10 km. We can see that the irregular shape of the nucleus of 67P is significantly influencing the lateral dust transport to the nightside.

side and nightside contributions have also been calculated and all plots have been normalized to 1 at 10 km for ease of comparison. The azimuthal average drops rapidly with distance and reaches its asymptotic value around 8–9 km from the centre of the sphere. The nightside component to the azimuthal average shows a rising value with distance. There is no emission from the nightside of the sphere but non-radial flow transfers dust to the nightside hemisphere and can be seen in the contribution to azimuthal average.

In Fig. 16 (right), the same calculation has been performed but with the shape model of 67P. One can see that the shape has some influence on the rate at which dust is transferred to the nightside hemisphere: The irregular shape of 67P, which features a lot of surface area not orthogonal to the radial direction from the comet centre, permits lateral dust transport more easily than in the spherical case where the dust is leaving the comet perpendicular to the surface.

The azimuthal average cannot be computed down to the surface because of the irregular shape. Hence, we miss a lot of the acceleration region and so the maximum value of the azimuthal average is not as high as in the spherical case. However, the fundamental behaviour of the azimuthal average is identical to the spherical case and to the behaviour of the azimuthal average observed in dust outflow analysis of OSIRIS images.

When studying the ratio of particles returning to the nucleus, we clearly see a dependency on particle size in simulation results (as expected). Because gravity is acting more strongly on the big-

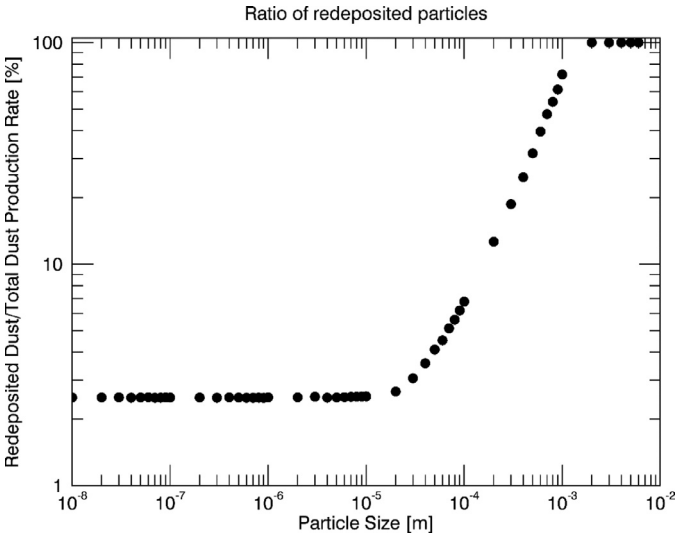

Fig. 17. Ratio of the redeposited dust on the nucleus to the total dust mass production rate. The dust solution was calculated for different particle sizes on a gas simulation with 1.5 kg s^{-1} gas production rate and a gas to dust production rate ratio of 1. For particle sizes smaller than 10^{-5} m we see that gravity does not play a dominant role and most of the particles are escaping from the comet. Particles above 10^{-3} m are not escaping anymore but are to 100% captured in ballistic trajectories and eventually redeposited on the comet surface.

ger and therefore heavier particles we expect to get higher rates of back-falling particles for simulation calculations with a larger particle size.

In a simulation with a gas production rate of 1.5 kg/s and a gas to dust production rate ratio of 1, we calculated the ratios of redeposited particles to the total amount of dust particles in the simulation for different particle sizes. In the simulation the shape model of 67P was used. The results are shown in Fig. 17. For particle sizes smaller than 10 µm we see that gravity does not play a dominant role and most of the particles are escaping from the comet. The constant value of about 2.5% redeposited dust particles is probably an effect of the irregular shape of the nucleus and originates primarily from the neck region where particles are lifted from one cliff and redeposited on the opposite cliff without necessarily being influenced by gravity.

Gravity starts to play a role for dust particles larger than 10 µm and particles larger than 1 mm do not escape from the comet at all in this model. They are captured in ballistic trajectories and redeposited onto the surface. This also means that more particles are appearing on the nightside because ballistic particle trajectories cause lateral dust transport.

5.4. The non-symmetric case and deviations from point source geometry

The study of dust profiles is an accepted approach for studying the dust outflow behaviour for comets. The difficulty is to define the profiles in a meaningful way such that unambiguous and reproducible results are guaranteed. Dust profiles along simple lines on the image plane lead to difficulties because they are extremely sensitive to the spatially fine structure of the coma and the orientation of the profile line. In Fig. 18 (right) we clearly see the effects of varying the azimuthal angle of different radial profile lines on the shape of the dust profiles in a relatively simple model. The changes in the behaviour of the dust profiles are significant and the example demonstrates that the deduction of a general behaviour of the dust outflow from single line profiles is not a straightforward approach if it is possible at all. The simulation image used in this example (Fig. 18 left) was generated with only acceleration of gas and dust from the surface and the shape effect of the irregular nucleus influencing the final structure of the coma.

Studying dust outflow with the azimuthal average poses a way of avoiding the main problems that arise with single line profiles. In the azimuthal average approach, integrations of the dust coma along circular paths around the nucleus (corresponding to closed cylindrical surfaces in full 3D) make sure that no dust is lost from the analysis. Dispersing or overlapping jets due to geometry or comet dynamics on the image plane do not cause problems in the analysis. The resulting profiles of azimuthal average reflect the general dust outflow behaviour and provide unambiguous results, which can be easily compared to other profile curves.

The numerical model is especially useful to study the isolated effects of single processes or coma characteristics on the azimuthal average. This might help in the future to determine the specific scale lengths of physical processes at work in the inner coma and possibly identify them in real observation profiles.

5.5. The starting point of the linear regime

We calculated the starting point of the linear behaviour for simulation images from model calculations on a simulation grid covering a radial domain of 20 km around the shape of comet 67P. For the calculations we used the same method that we used in the starting point calculations for OSIRIS images described in Section 3.3. The model simulations were set up with different dust particle sizes to study the starting point as a function of dust particle size. Our results are shown in Fig. 19. We find the starting point of the linear regime to lie between 11.7 km and 12.5 km for our simulated dust coma. This agrees very well (inside the calculated error) with the starting point that we estimated from OSIRIS image analysis in Section 4.4.

We notice a dependency of the starting point on the dust particle size, although the variations are quite small. Dust particles with sizes between 0.1 and 1 µm seem to show approximately the same behaviour independent of particle size and free-radial outflow can be assumed beyond distances of 12 km from the nucleus centre. Below that size range, the starting point and the particle size seem to scale almost proportionally (i.e. smaller particles have a smaller starting point) and the same applies for particles larger than 1 µm. This implies that the smaller particles reach their final outflow velocity earlier. In the increasing starting point values for larger particles we might already see the influence of gravity on the particles. When gravitationally bound particles in ballistic trajectories contribute significantly to the azimuthal average in the region close to the nucleus, i.e. in the “acceleration region”, the decrease of the azimuthal average close to the nucleus would be less steep. Because we defined the starting point of the linear regime as the point at which the contribution of the power-law in the fit to the azimuthal average drops below the 1% level, the starting point would be shifted towards larger distances for a more moderately decreasing power-law in the “acceleration region” as we observe for larger dust particles.

6. Discussion and conclusions

The conclusions from the study can be summarized as follows:

From analyses of many single images, we have identified the typical behaviour of the azimuthal average, $\bar{A}$, with impact parameter, b. The $\bar{A}$-curves can be divided in two different regions: the “acceleration region” close to the nucleus where the azimuthal average profile decreases more steeply than a “1/r law”, and the linear regime where the profile converges towards constant behaviour at larger impact parameters.

For 67P, the azimuthal average, computed as the integral of the product of dust reflectance and impact parameter over con-

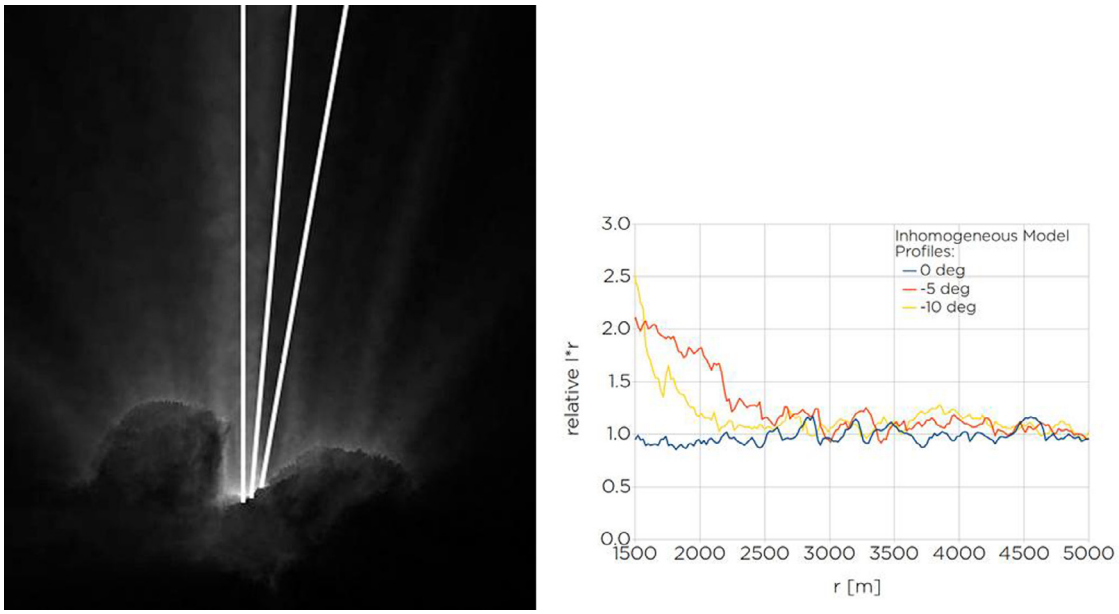

Fig. 18. Simple example showing deviations from 1/r in profiles. This is a model with no fragmentation, no sublimation effects and no optical depths. The plot to the right shows the values of $I{\cdot}r$ (in arbitrary units). Only deviations from point source geometry and the acceleration of the gas/dust is included. Variations in adjacent profiles clearly demonstrate that profiles do not provide a straightforward interpretation of the outflow.

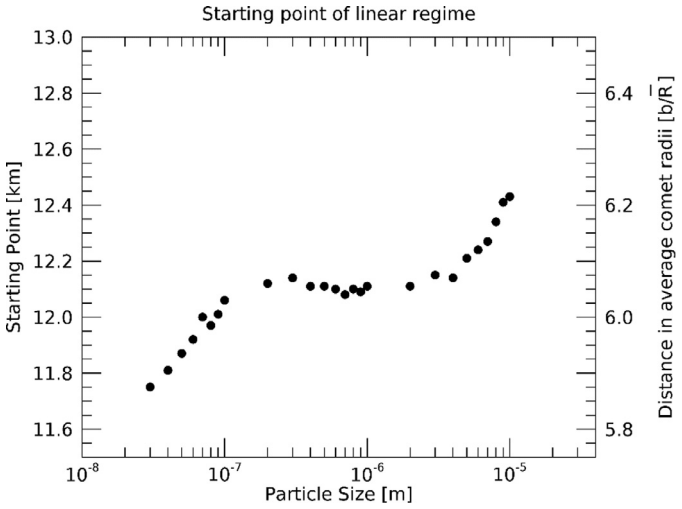

Fig. 19. Starting point of the linear regime of the Ā-curve for the full angle analysis derived from simulation images generated on a simulation grid with a 20 km domain around the shape model of comet 67P. We used a gas production rate of 1.5 kg/s in our simulation and a gas to dust production rate ratio of 1. The simulation images were generated for a viewing geometry with a phase angle of 90° The same model calculations were executed for different particle sizes and the starting point was then calculated using the same method as described in the single image analysis in Section 3.3.

centric circles around the nucleus, decreases with increasing impact parameter in the first few kilometres. This is in the opposite sense to the behaviour of the azimuthal average observed at comet 1P/Halley (Thomas and Keller, 1990). This indicates that the dominant physical processes governing the dust brightness distribution within the first 6–10 comet radii from the nucleus centre are fundamentally different. In the case of 1P/Halley, particle fragmentation into optically active daughter products or optical depth effects (or a combination of the two) were dominant. In the case of 67P, deviations from point source geometry, particle acceleration, particle fragmentation into optically inactive daughter products or sublimation (or a combination of two or more of these processes) were dominant.

A large number of OSIRIS images were analysed and the essential information from the single image analysis was collected into a database. This enables statistical analysis of selected parameters over an extended dataset. We studied the dust outflow behaviour in the linear regime more closely by performing a statistical analysis regarding the distribution of the linear slope parameter w of a fit to the Ā-curves. We found that the distributions of the linear slope gradient closely follow Gaussian distributions with mean values that are closer to zero than 2 σ'_w indicating adherence to a 1/r law. There is good agreement between the distributions calculated separately for the NAC and the WAC images. The NAC uses broader bandwidth filters while the WAC uses narrow-band filters. The agreement indicates that the WAC filters used for the analysis are not significantly affected by gas emissions within the band. A distribution computed using the OI (630 nm) filter in the WAC does however show a significant difference with a brightness profile less steep than 1/r. We conclude that gas is a major “contaminant” in this filter.

We define the “starting point” as the impact parameter where the ratio of the linear contribution to the total fit function value exceeds 99%, which means that the contributions from the power-law used to fit the acceleration region has dropped below 1%. The analysis showed that the average starting point of the 1/r behaviour is at 11.9 ± 2.8 km corresponding to 6 comet radii from the nucleus centre and we suggest this as a means of defining the distance beyond which 1/r behaviour for the dust can be assumed. However, it should be noted that the starting point is probably time dependent and the average value over the whole time period merely presents a typical value.

Splitting the integration into two and integrating over the dayside and nightside separately gives some additional insights in the physical processes ongoing in the inner coma (e.g. we can see strong indications for lateral dust transport). The mean value of the distribution for the WAC dayside analysis, which includes most of the coma activity and is not biased by shadowing effects, shows a tendency for falling Ā-curves, hinting that some of the dust may be transferred to the nightside hemisphere.

The dust flow behaviour on the nightside significantly differs from the behaviour observed on the dayside or for the full azimuthal angle integration of dust reflectance around the nucleus. Statistical analysis of the slope gradients on the nightside show that in a majority of images dust reflectance on the nightside decreases less steeply than a "1/r law".

The observed differences between the behaviour on the dayside and nightside are probably caused by a combination of two effects. On the one hand, the nightside coma is partly shadowed from sunlight by the nucleus. Because the ratio of shadowed coma to illuminated coma is large close to the nucleus but decreases with increasing impact parameter this leads to rising $\bar{A}$-curves on the nightside. We have estimated the deviation from 1/r on the nightside caused by shadowing from the nucleus and found a value of at maximum +1.2%/km for the rising slope due to this effect. This would be just about sufficient to explain the nightside observation in isolation. However, we expect a similar behaviour to arise from lateral flow of particles from the dayside to the nightside. Such a process would explain the dayside behaviour as well and model calculations support this interpretation by reproducing the behaviour of the azimuthal average well.

From analysis of our fit value of the offset parameter, z, we have calculated Afρ values of the coma of 67P as a function of time. The values we found agree well with Afρ values for 67P from the paper of Agarwal et al. (2007) and are consistent with the results of Snodgrass et al. (2016) when the phase angles of the observations are accounted for. In our analysis we found a maximum Afρ value of about 210 cm at 20 days post-perihelion when data is normalized to a phase angle of 90°.

The numerical model used in this paper only included effects from the irregular shape of the comet nucleus and acceleration of dust particles through gas drag and gravity. We show that other effects such as fragmentation or sublimation are not required. These processes cannot be ruled out but application of Ockham's razor demands that they are not required to explain the results herein.

With the help of the simulations it is possible to study effects of isolated processes, as demonstrated above, or a special combination of two or more processes on the dust outflow behaviour. This can help in the future with the differentiation between processes at work in the "acceleration region" where we observe deviations from 1/r outflow behaviour. By studying effects of sublimation or fragmentation in the same manner as we studied the effects of acceleration on the azimuthal average in this paper it can help to determine the specific scale lengths of physical processes and thereby with the interpretation of results from data analysis.

Acknowledgements

The team from the University of Bern is supported through the Swiss National Science Foundation and through the NCCR PlanetS. The project has also received funding from the European Union's Horizon 2020 research and innovation programme under grant agreement No. 686709. This work was supported by the Swiss State Secretariat for Education, Research and Innovation (SERI) under contract number 16.0008-2. The opinions expressed and arguments employed herein do not necessarily reflect the official views of the Swiss Government.

OSIRIS was built by a consortium led by the Max-Planck-Institut für Sonnensystemforschung, Göttingen, Germany, in collaboration with CISAS, University of Padova, Italy, the Laboratoire d'Astrophysique de Marseille, France, the Instituto de Astrofísica de Andalucia, CSIC, Granada, Spain, the Scientific Support Office of the European Space Agency, Noordwijk, The Netherlands, the Instituto Nacional de Técnica Aeroespacial, Madrid, Spain, the Universidad Politéchnica de Madrid, Spain, the Department of Physics and Astronomy of Uppsala University, Sweden, and the Institut für Datentechnik und Kommunikationsnetze der Technischen Universität Braunschweig, Germany.

We thank Diana Gamborino for providing the computer code used in our calculations of the Chamberlain model.

Appendix A. Additional examples of single image analysis

In this appendix we present some more examples of single OSIRIS images analysed using our approach as described in Section 3.3. The selected images show examples throughout the whole period of image acquisition during the year 2015. We show images from different time periods, different filters and the two different cameras NAC and WAC. We will point out the differences between the images and address the difficulties during analysis (Figs A.1–A.4).

Every example contains the original OSIRIS image (a) with enhanced contrast to make the faint coma visible. We then show the profile of the azimuthal average (b) and the $\bar{A}$ -curves (c) for the full angle (black), the dayside (red) and the nightside analysis (blue) and the fits to the $\bar{A}$-curves in orange.

It should be noted that the scale on the abscissa is individually scaled and is intended to increase visibility of small deviations from 1/r. A list of example images discussed in this paper is given below. The first image 1) is the example image used in Section 3.3 and is not repeated here.

In two additional examples at the end we will show a comparison of profile curves from images acquired with the three narrowband WAC filter combinations 16, 17, and 18. We will focus on the effects of gas contribution visible in filter 17.

Full image name of OSIRIS images discussed in this paper (*Table 2*):

(1) WAC_2015-08-05T13.01.46.512Z_IDB0_1397549000_F18
(2) WAC_2015-02-09T16.32.10.070Z_IDB0_1397549000_F18
(3) WAC_2015-05-06T22.15.54.857Z_IDB0_1397549000_F17
(4) NAC_2015-08-26T18.19.26.156Z_IDB0_1397549001_F24
(5) NAC_2015-09-29T02.47.23.743Z_IDB0_1397549000_F22
(6) WAC_2015-07-25T08.08.46.806Z_IDB0_1397549000_F18
(7) WAC_2015-07-25T08.09.02.479Z_IDB0_1397549001_F17
(8) WAC_2015-08-01T17.13.33.341Z_IDB0_1397549000_F18
(9) WAC_2015-08-01T17.13.41.502Z_IDB0_1397549001_F16

Example image #2

In this first additional example (Fig. A.1) the dust coma is visible inside a radius of approximately 9 km projected distance. The coma is still faint: the azimuthal average multiplied with the impact parameter for the dayside is here below the level of the nightside curve for images around perihelion (compare Fig. 8). We see that the $\bar{A}$-profile outside the acceleration region is slightly curved but shows almost linear behaviour beyond impact parameters of about 5 km. The $\bar{A}$-curve for the full angle is slightly rising, whereas the dayside analysis suggests a dust outflow behaviour following a "1/r law". The $\bar{A}$ curve for the nightside is clearly rising. We observe this behaviour in many of the images and it is probably an effect of non-radial dust flow towards the nightside possibly in combination with effects of shadowing by the nucleus.

Example image #3

The image (Fig. A.2) was acquired around equinox in May 2015. We see here an example which has a viewing geometry on the comet with a lower phase angle of 63.8°. The profile analysis only extends out to impact parameters of about 8 km, although in the original image we see a much larger part of the coma in the upper half of the image. But because we need the full 2π integration around the comet for the full angle azimuthal average analysis and the nucleus is not located in the centre of the image we are limited to low impact parameters. In the $\bar{A}$-curves the acceleration region is not very pronounced and follows a rather flat decrease. The

Example image #2

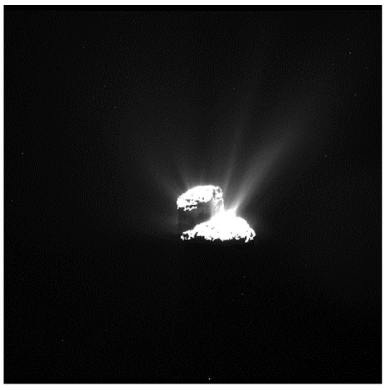

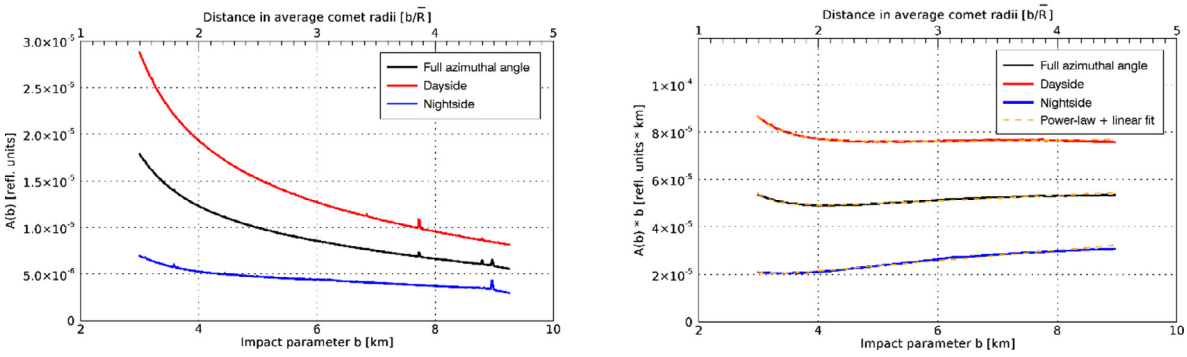

Fig. A.1. The original OSIRIS WAC image was taken on the 09.02.15 with filter 18 (Vis 610) and a phase angle of 87.5°.

Table 2
Image information extracted from the Osimana database for the example images that are shown in this paper. The numbers on the left side refer to the corresponding image in the list below.

#	Date	Camera	Filter	Heliocentric distance (AU)	Comet centric distance (km)	Phase angle (deg)
1	05.08.2015	WAC	Vis 610 (18)	1.25	255.69	89.49
2	09.02.2015	WAC	Vis 610 (18)	2.35	106.33	87.52
3	06.05.2015	WAC	OI (17)	1.70	159.53	63.80
4	26.08.2015	NAC	Blue (24)	1.25	407.24	81.57
5	29.09.2015	NAC	Orange (22)	1.37	1315.64	50.14
6	25.07.2015	WAC	Vis 610 (18)	1.26	183.67	89.99
7	25.07.2015	WAC	OI (17)	1.26	183.67	89.99
8	01.08.2015	WAC	Vis 610 (18)	1.25	211.22	89.51
9	01.08.2015	WAC	Na (16)	1.25	211.22	89.51

curves for the dayside and the full angle analysis converge towards slightly rising behaviour beyond impact parameters between 4 and 5 km. The nightside curve shows linear behaviour from the very beginning close to the comet surface and follows a slightly rising trend.

Example image #4

The example number 4 (Fig. A.3) shows a visible part of the dust coma out to impact parameters of about 7 km. The image was acquired on the 26.08.2015 at a heliocentric distance of 1.25 AU. The higher comet centric distance of 407.24 km allowed observations of the whole nucleus as well as a good part of the surrounding coma with the OSIRIS NAC. The $\bar{A}$-curves on the dayside and over the full angle are slightly decreasing and it is conceivable, that the dust in the visible part of the coma has not yet reached free-radial outflow conditions. On the nightside the $\bar{A}$-curve is almost perfectly constant from the very beginning of the profile close to the comet surface.

Example image #5

The next additional example (Fig. A.4) shows a visible part of the dust coma out to impact parameters of about 22.5 km. The image was acquired on the 29.09.2015 at a heliocentric distance of 1.37 AU. The very high comet centric distance of 1315.64 km allows for an unusually large field of view even for NAC images. The $\bar{A}$-curve on the dayside is slightly decreasing, while the full angle curve is almost constant at impact parameters larger than about 10 km. The viewing geometry of the situation with a low phase angle of 50.7° could lead to an enhanced brightness on the nightside due to dust reflectance from the dayside that appears on the nightside in the projection onto the image plane. In this example we see that the results from NAC images with a high field of view show the same behaviour for the azimuthal average as the WAC images, as expected, and we see that the dust outflow is converging towards a "1/r law" outflow behaviour.

Filter comparison F18/F17 (Example images #6 and #7)

The two OSIRIS images that are compared in Fig. A.5 and the two images compared in Fig. A.6 were acquired only seconds apart. Hence, the observation geometry for both images is the same but different filter combinations were used. Differences in the observed brightness profiles can therefore solely be explained by the difference in wavelength range observed with the two different filter combinations. Filter combination 16 (Na-filter) has a central wavelength at 590.7 nm and a bandwidth of 4.7 nm, filter combination 17 (OI-filter) has a central wavelength at 631.6 nm and a bandwidth of 4.0 nm, and filter combination 18 (Vis 610) has a

Example image #3

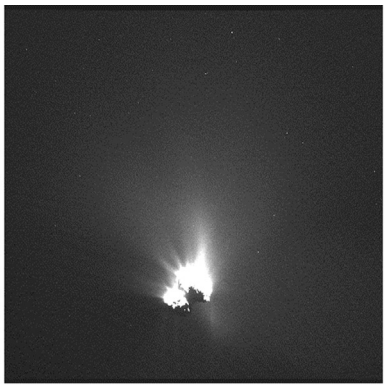

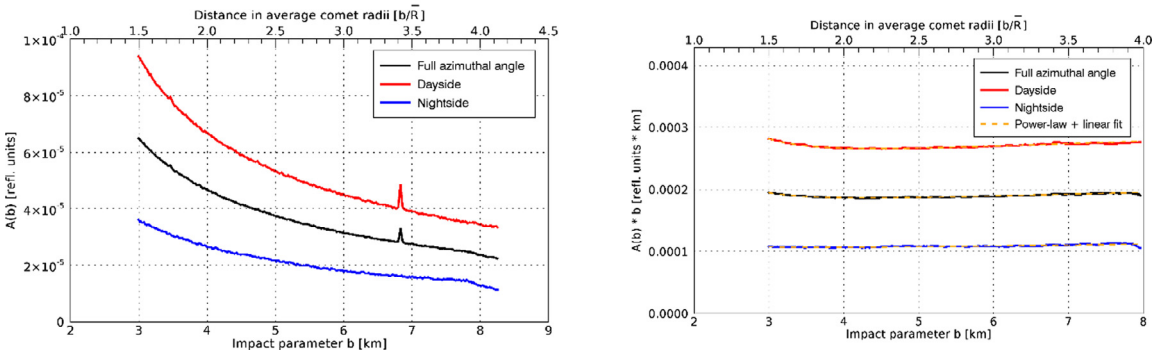

Fig. A.2. The original OSIRIS WAC image was taken on the 06.05.2015 with filter 17 (OI) and a phase angle of 63.80°.

Example image #4

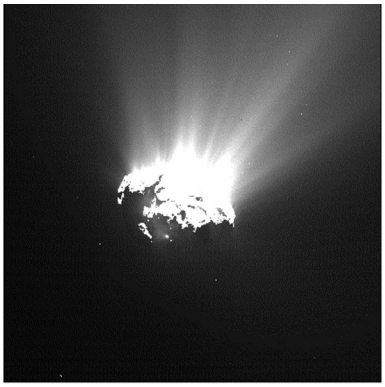

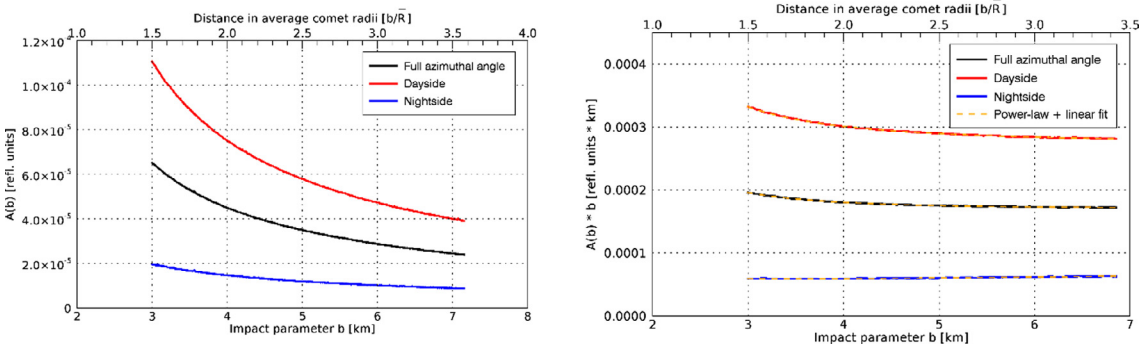

Fig. A.3. The original OSIRIS WAC image was taken on the 26.08.2015 with filter 24 (Blue) and a phase angle of 81.57°.

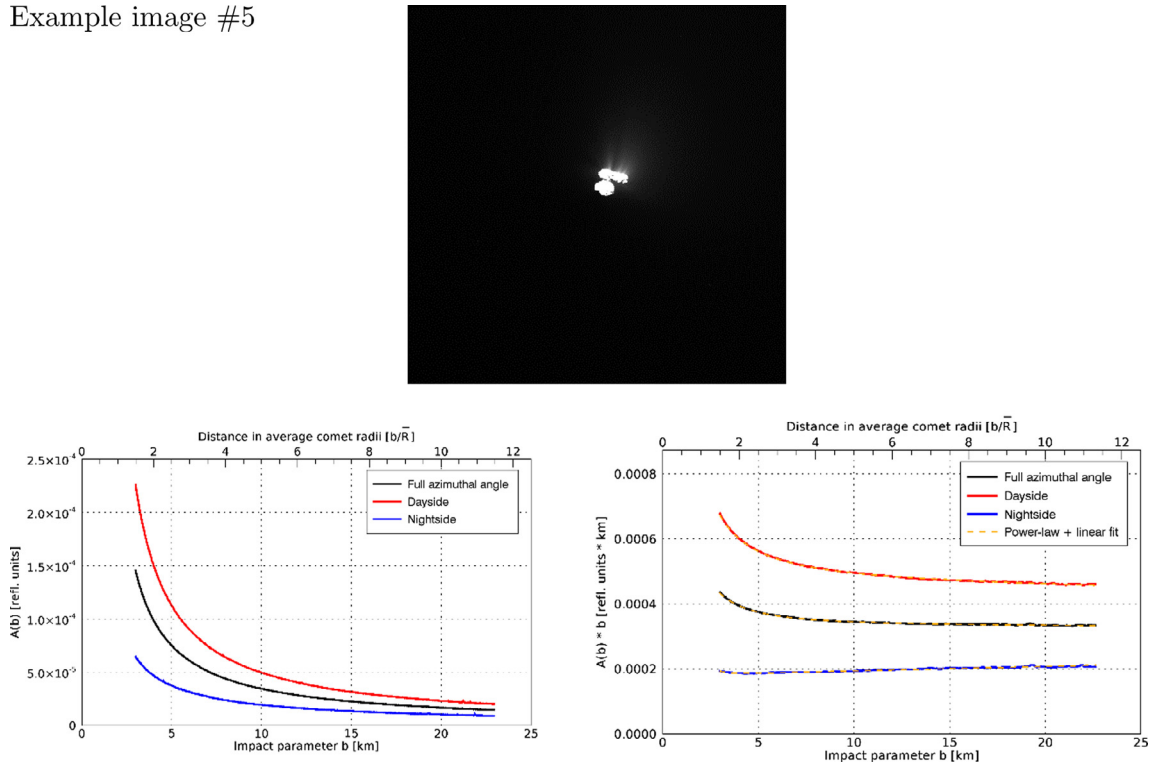

Fig. A.4. The original OSIRIS NAC image was taken on the 29.09.2015 with filter 22 and a phase angle of 50.7°.

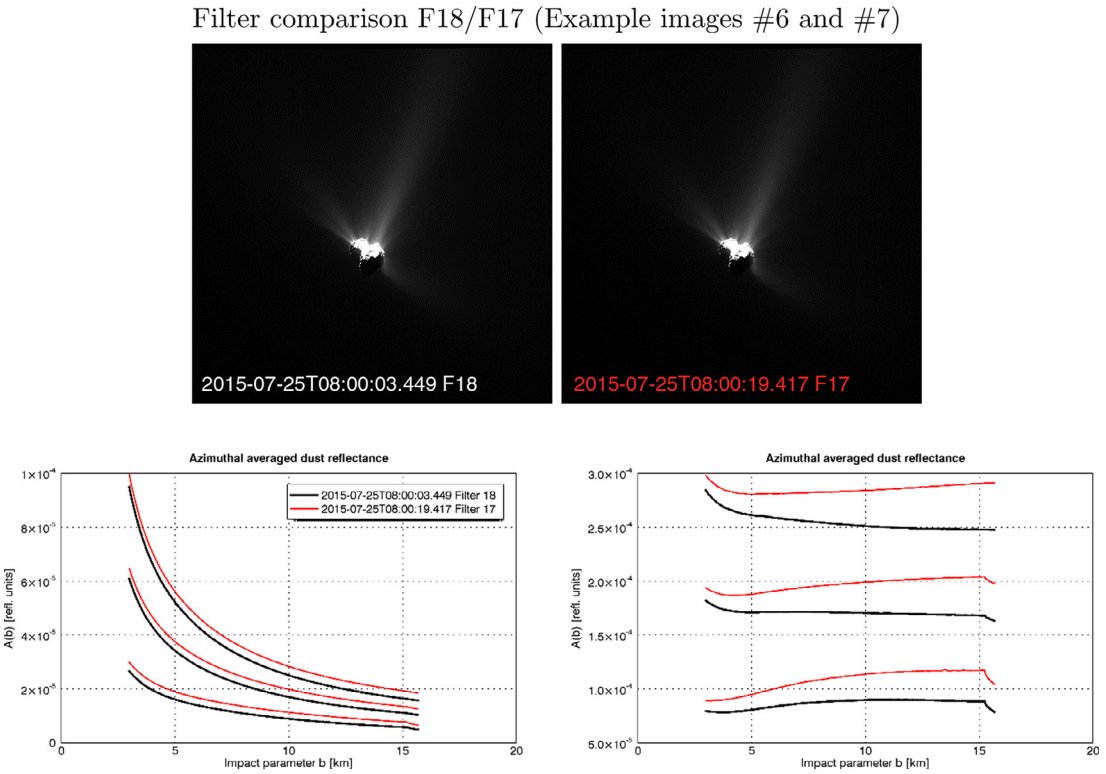

Fig. A.5. Comparison of two narrowband OSIRIS WAC images acquired with two different filter combinations, filter combination 18 (F18) and 17 (F17). The profile curves concerning the F18 image (left) are black in the diagrams below and the profile curves concerning the F17 image (right) are depicted in red. (For interpretation of the references to colour in this figure legend, the reader is referred to the web version of this article.)

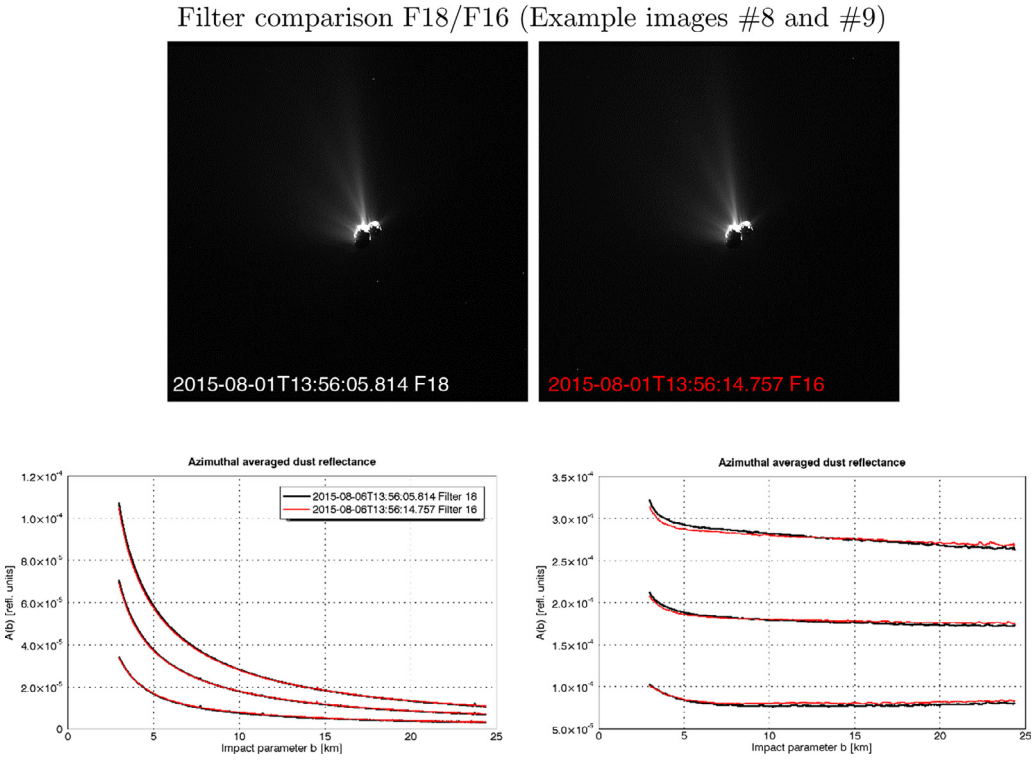

Fig. A.6. Comparison of two narrowband OSIRIS WAC images acquired with two different filter combinations, filter combination 18 (F18) and 16 (F16). The profile curves concerning the F18 image (left) are black in the diagrams below and the profile curves concerning the F16 image (right) are depicted in red. (For interpretation of the references to colour in this figure legend, the reader is referred to the web version of this article.)

central wavelength at 612.6 and a bandwidth of 9.8 nm (Keller et al., 2007). The dust coma brightness is not expected to change significantly in observations with filter combinations 16, 17 or 18 because they cover wavelength bands in a similar wavelength range.

However, in the profile curves in Fig. A.5 we observe a significant difference in the brightness of the coma: the image acquired with F17 shows more brightness in the inner coma than the image acquired with F18. The $\bar{A}$-curves for the F17 image show a clear rising tendency. We conclude that we observe a significant amount of gas emission contributions (oxygen emission) to the coma brightness in OSIRIS image acquired with F17 (see also Bodewits et al., 2016).

Comparison of images acquired with F18 and F16 (e.g. Fig. A.6) show no significant differences in coma brightness or coma behaviour and we therefore conclude that the narrowband WAC filter combinations 16 and 18 are not biased by gas contributions.

Filter comparison F18/F16 (Example images #8 and #9)

Supplementary materials

Supplementary material associated with this article can be found, in the online version, at doi:10.1016/j.icarus.2018.03.010.

References

Agarwal, J., Müller, M., Grün, E., 2007. Dust environment modelling of comet 67P/Churyumov–Gerasimenko. Space Sci. Rev. 128, 79–131.

Agarwal, J., A'Hearn, M.F., Vincent, J.-B., et al., 2016. Acceleration of individual, decimetre-sized aggregates in the lower coma of comet 67P/Churyumov–Gerasimenko. Mon. Not. R. Astron. Soc. 462, 78–88.

A'Hearn, M.F., Schleicher, D.G., Millis, R.L., et al., 1984. Comet bowell 1980b. Astron. J. 89, 579–591.

Bertini, I., La Forgia, F., Tubiana, C., Güttler, C., Fulle, M., Moreno, F., Frattin, E., Kovacs, G., Pajola, M., Sierks, H., Barbieri, C., Lamy, P., Rodrigo, R., Koschny, D., Rickman, H., Keller, H.U., Agarwal, J., A'Hearn, M.F., Barucci, M.A., Bertaux, J.-L., Bodewits, D., Cremonese, G., Da Deppo, V., Davidsson, B., Debei, S., De Cecco, M., Drolshagen, E., Ferrari, S., Ferri, F., Fornasier, S., Gicquel, A., Groussin, O., Gutierrez, P.J., Hasselmann, P.H., Hviid, S.F., Ip, W.-H., Jorda, L., Knollenberg, J., Kramm, J.R., Kührt, E., Küppers, M., Lara, L.M., Lazzarin, M., Lin, Z.-Y., Moreno, J.J.Lopez, Lucchetti, A., Marzari, F., Massironi, M., Mottola, S., Naletto, G., Oklay, N., Ott, T., Penasa, L., Thomas, N., Vincent, J.B., 2017. The scattering phase function of comet 67P/Churyumov–Gerasimenko coma as seen from the Rosetta/OSIRIS instrument. Mon. Not. R. Astron. Soc. 469, 404–415.

Bodewits, D., Lara, L.M., A'Hearn, M.F., La Forgia, F., Gicquel, A., Kovacs, G., Knollenberg, J., Lazzarin, M., Lin, Z.-Y., Shi, X., Snodgrass, C., Tubiana, C., Sierks, H., Barbieri, C., Lamy, P.L., Rodrigo, R., Koschny, D., Rickman, H., Keller, H.U., Barucci, M.A., Bertaux, J.-L., Bertini, I., Boudreault, S., Cremonese, G., Da Deppo, V., Davidsson, B., Debei, S., De Cecco, M., Fornasier, S., Fulle, M., Groussin, O., Gutiérrez, P.J., Güttler, C., Hviid, S.F., Ip, W.-H., Jorda, L., Kramm, J.-R., Kührt, E., Küppers, M., Lòpez-Moreno, J.J., Marzari, F., Naletto, G., Oklay, N., Thomas, N., Toth, I., Vincent, J.-B., 2016. Changes in the physical environment of the inner coma of 67P/Churyumov–Gerasimenko with decreasing heliocentric distance. Astron. J. 152, 130.

Boice, D.C., Soderblom, L.A., Britt, D.T., et al., 2002. The deep space 1 encounter with comet 19p/borrelly. Earth Moon Planets 89, 301–324.

Cercignani, C., 2000. Rarefied Gas Dynamics. Cambridge University Press.

Chamberlain, J.W., 1963. Planetary coronae and atmospheric evaporation. Planet. Space Sci. 11, 901–960.

Chamberlain, J.W., Hunten, D.M., 1987. Theory of Planetary Atmospheres. International geophysical series, 36, 2nd Ed. Academic Press, INC..

Coradini, A., Capaccioni, F., Drossart, P., Arnold, G., Ammannito, E., Angrilli, F., Barucci, A., Bellucci, G., Benkhoff, J., Bianchini, G., Bibring, J.P., Blecka, M., Bockelee-Morvan, D., Capria, M.T., Carlson, R., Carsenty, U., Cerroni, P., Colangeli, L., Combes, M., Combi, M., Crovisier, J., De Sanctis, M.C., Encrenaz, E.T., Erard, S., Federico, C., Filacchione, G., Fink, U., Fonti, S., Formisano, V., Ip, W.H., Jaumann, R., Kuehrt, E., Langevin, Y., Magni, G., McCord, T., Mennella, V., Mottola, S., Neukum, G., Palumbo, P., Piccioni, G., Rauer, H., Saggin, B., Schmitt, B., Tiphene, D., Tozzi, G., 2007. VIRTIS: an imaging spectrometer for the rosetta mission. Space Sci. Rev. 128, 529–559.

Crifo, J.-F., Rodionov, A.V., 1997. The dependence of the circumnuclear coma structure on the properties of the nucleus. I. Comparison between a homogeneous and an inhomogeneous spherical nucleus with application to P/Wirtanen. Icarus 127, 319–353.

Crifo, J.-F., Loukianov, G.A., Rodionov, A.V., Zakharov, V.V., 2005. Direct Monte Carlo and multifluid modeling of the circumnuclear dust coma. Spherical grain dynamics revisited. Icarus 176, 192–219.

Davidsson, B.J.R., Gutiérrez, P.J., Sierks, H., Barbieri, C., Lamy, P.L., Rodrigo, R., Koschny, D., Rickman, H., Keller, H.U., Agarwal, J., A'Hearn, M.F., Barucci, M.A., Bertaux, J.-L., Bertini, I., Bodewits, D., Cremonese, G., Da Deppo, V., Debei, S., De Cecco, M., Fornasier, S., Fulle, M., Groussin, O., Güttler, C., Hviid, S.F., Ip, W.-H., Jorda, L., Knollenberg, J., Kovacs, G., Kramm, J.-R., Kührt, E., Küppers, M., La Forgia, F., Lara, L.M., Lazzarin, M., Lopez Moreno, J.J., Lowry, S., Magrin, S.,

Marzari, F., Michalik, H., Moissl-Fraund, R., Naletto, G., Oklay, N., Pajola, M., Snodgrass, C., Thomas, N., Tubiana, C., Vincent, J.-B., 2015. Orbital elements of the material surrounding comet 67P/Churyumov–Gerasimenko. Astron. Astrophys. 583, A16.

Davidsson, B.J.R., Gulkis, S., Alexander, C., Allmen, P.v., Kamp, L., Lee, S., Warell, J., 2010. Gas kinetics and dust dynamics in low-density comet comae. Icarus 210, 455–471.

Drolshagen, E., Ott, T., Koschny, D., Güttler, C., Tubiana, C., Agarwal, J., Sierks, H., Barbieri, C., Lamy, P.I., Rodrigo, R., Rickman, H., A'Hearn, M.F., Barucci, M.A., Bertaux, J.-L., Bertini, I., Cremonese, G., Da Deppo, V., Davidsson, B., Debei, S., Cecco, M.D., Deller, J., Feller, C., Fornasier, S., Fulle, M., Gicquel, A., Groussin, O., Gutiérrez, P.J., Hofmann, M., Hviid, S.F., Ip, W.-H., Jorda, L., Keller, H.U., Knollenberg, J., Kramm, J.R., Kührt, E., Küppers, M., Lara, L.M., Lazzarin, M., Moreno, J.J.L., Marzari, F., Naletto, G., Oklay, N., Shi, X., Thomas, N., Poppe, B., 2017. Distance determination method of dust particles using rosetta OSIRIS NAC and WAC data. Planet. Space Sci. 143, 256–264.

Fink, U., Rubin, M., 2012. The calculation of Afρ and mass loss rate for comets. Icarus 221, 721–734.

Fulle, M., Della Corte, V., Rotundi, A., 2015. Dust measurements in the coma of comet 67P/Churyumov–Gerasimenko inbound to the Sun between 3.7 and 3.4 AU. In: Proceedings of the Lunar Planetary Science Conference, 46, p. 2420.

Fulle, M., Marzari, F., Della Corte, V., et al., 2016. Evolution of the dust size distribution of comet 67P/Churyumov–Gerasimenko from 2.2 AU to perihelion. Astrophys. J. 821, 19.

Gicquel, A., Vincent, J.-B., Agarwal, J., et al., 2016. Sublimation of icy aggregates in the coma of comet 67P/Churyumov–Gerasimenko detected with the OSIRIS cameras on board Rosetta. Mon. Not. R. Astron. Soc. 462, 57–66.

Gombosi, T.I., Cravens, T.E., Nagy, A.F., 1985. Time-dependent dusty gasdynamical flow near cometary nuclei. Astrophys. J. 293, 328–341.

Gulkis, S., Frerking, M., Crovisier, J., et al., 2007. MIRO: microwave instrument for rosetta orbiter. Space Sci. Rev. 128, 561–597.

Gulkis, S., Allen, M., von Allmen, P., et al., 2015. Subsurface properties and early activity of comet 67P/Churyumov–Gerasimenko. Science 347, 709.

Huebner, W.F., Boice, D.C., Reitsema, H.J., Delamere, W.A., Whipple, F.L., 1988. A model for intensity profiles of dust jets near the nucleus of Comet Halley. Icarus 76, 78–88.

Keller, H.U., Curdt, W., Kramm, J.-R., Thomas, N., (1994). Images of the nucleus of Comet Halley. Volume 1: Images obtained by the Halley Multicolour Camera (HMC) on board the Giotto spacecraft, ESA SP-1127.

Keller, H.U., Barbieri, C., Lamy, P., et al., 2007. OSIRIS – the scientific camera system onboard rosetta. Space Sci. Rev. 128, 433–506.

Keller, H.U., Mottola, S., Hviid, S.F., et al., 2017. Seasonal mass transfer on the nucleus of comet 67P/Churyumov–Gerasimenko. MNRAS 469, 357–371.

Konno, I., Huebner, W.F., Boice, D.C., 1989. A model of dust fragmentation in the near-nucleus jet-like features in Comet P/Halley. Icarus 101, 84–94.

Liao, Y., 2017. Global explorations of inner neutral gas coma of comet 67P/Churyumov–Gerasimenko with DSMC approach Ph.D. thesis. University of Bern, Switzerland.

Lien, D.J., 1990. Dust in comets. I – thermal properties of homogeneous and heterogeneous grains. Astrophys. J. 355, 680–692.

Lin, Z.-Y., Ip, W.-H., Lai, I.-L., et al., 2015. Morphology and dynamics of the jets of comet 67P/Churyumov–Gerasimenko: early-phase development. Astron. Astrophys. 583, A11.

Lin, Z.-Y., Lai, I.-L, Su, C.-C., et al., 2016. Observations and analysis of a curved jet in the coma of comet 67P/Churyumov–Gerasimenko. Astron. Astrophys. 588, L3.

Markwardt, C.B., 2009. Non-linear least-squares fitting in IDL with MPFIT. In: Proceedings of the Astronomical Data Analysis Software and Systems XVIII, p. 251.

Marschall, R., Su, C.C., Liao, Y., et al., 2016. Modelling observations of the inner gas and dust coma of comet 67P/Churyumov–Gerasimenko using ROSINA/COPS and OSIRIS data: first results. Astron. Astrophys. 589, A90.

Marschall, R., Mottola, S., Su, C.C., Liao, Y., Rubin, M., Wu, J.S., Thomas, N., Altwegg, K., Sierks, H., Ip, W.-H., Keller, H.U., Knollenberg, J., Kührt, E., Lai, I.L., Skorov, Y., Jorda, L., Preusker, F., Scholten, F., Vincent, J.-B., the OSIRIS and ROSINA teams, 2017. Cliffs vs. Plains: can ROSINA/COPS and OSIRIS data of comet 67P/Churyumov–Gerasimenko in autumn 2014 constrain inhomogeneous outgassing? Astron. Astrophys. 605, A112.

Möhlmann, D., 1994. Surface regolith and environment of comets. Planet. Space Sci. 42, 933–937.

Ott, T., et al., 2017. Dust mass distribution around comet 67P/Churyumov–Gerasimenko determined via parallax measurements using Rosetta's OSIRIS cameras. Mon. Not. R. Astron. Soc. 469, S276–S284.

Preusker, F., Scholten, F., Matz, K.-D., Roatsch, T., Hviid, S.F., Mottola, S., Knollenberg, J., Kührt, E., Pajola, M., Oklay, N., Vincent, J.-B., Davidsson, B., A'Hearn, M.F., Agarwal, J., Barbieri, C., Barucci, M.A., Bertaux, J.-L., Bertini, I., Cremonese, G., Da Deppo, V., Debei, S., De Cecco, M., Fornasier, S., Fulle, M., Groussin, O., Gutiérrez, P.J., Güttler, C., Ip, W.-H., Jorda, L., Keller, H.U., Koschny, D., Kramm, J.R., Küppers, M., Lamy, P., Lara, L.M., Lazzarin, M., Lopez Moreno, J.J., Marzari, F., Massironi, M., Naletto, G., Rickman, H., Rodrigo, R., Sierks, H., Thomas, N., Tubiana, C., 2017. The global meter-level shape model of comet 67P/Churyumov–Gerasimenko. Astron. Astrophys. 607, L1.

Reitsema, H.J., Delamere, W.A., Williams, A.R., et al., 1989. Dust distribution in the inner coma of Comet Halley – comparison with models. Icarus 81, 31–40.

Richter, K., Keller, H.U., 1995. On the stability of dust particle orbits around cometary nuclei. Icarus 114, 355–371.

Rotundi, A., Sierks, H., Della Corte, V., Fulle, M., et al., 2015. Coma dust environment observed by GIADA during the perihelion of 67P/Churyumov–Gerasimenko. Science 347 (6220), aaa3905.

Schloerb, F.P., Keihm, S., von Allmen, P., et al., 2015. MIRO observations of subsurface temperatures of the nucleus of 67P/Churyumov–Gerasimenko. Astron. Astrophys. 583, 11.

Sierks, H., Barbieri, C., Lamy, P.L., et al., 2015. On the nucleus structure and activity of comet 67P/Churyumov–Gerasimenko. Science 347, 1044.

Snodgrass, C., Opitom, C., de Val-Borro, M., Jehin, E., Manfroid, J., Lister, T., Marchant, J., Jones, G.H., Fitzsimmons, A., Stale, I.A., Smith, R.J., Jermak, H., Granzer, T., Meech, K.J., Rousselot, P., Levasseur-Regourd, A.-C., 2016. The perihelion activity of comet 67P/Churyumov-Gerasimenko as seen by robotic telescopes. MNRAS 462, 138–145.

Szego, K., Toth, I., Sagdeev, R.Z., Szatmary, Z., Smith, B.A., Kondor, A., Merenyi, E., 1989. Dust photometry in the near nucleus region of Comet Halley. Adv. Space Res. 9 (3), 89–92.

Su, C.C., (2013). Parallel Direct Simulation Monte Carlo (DSMC) Methods for Modeling Rarefied Gas Dynamics, Ph.D. thesis, National Chiao Tung Univ., Taiwan.

Tenishev, V., Combi, M., Davidsson, B., 2008. A global kinetic model for cometary comae: the evolution of the coma of the rosetta target comet Churyumov–Gerasimenko throughout the mission. Astrophys. J. 685, 659–677.

Thomas, N., Keller, H.U., 1990. Interpretation of the inner coma observations of comet P/Halley by the Halley Multicolor Camera. Ann. Geophys. 8, 147–165.

Thomas, N., Davidsson, B., El-Maarry, M.R., et al., 2015. Redistribution of particles across the nucleus of comet 67P/Churyumov–Gerasimenko. Astron. Astrophys. 583, A17.

Tubiana, C., Güttler, C., Kovacs, G., et al., 2015. Scientific assessment of the quality of OSIRIS images. Astron. Astrophys. 583, A46.

Wu, J.-S., Lian, Y., 2003. Parallel three-dimensional direct simulation Monte-Carlo method and its applications. Comput. Fluids 32, 1133.

Wu, J.-S., Tseng, K.-C., 2005. Parallel DSMC method using dynamic domain decomposition. Int. J. Numer. Methods Eng. 63, 37–76.

Wu, J.-S., Tseng, K.-C., Wu, F.-Y., 2004. Parallel three-dimensional DSMC method using mesh refinement and variable time-step scheme. Comput. Phys. Commun. 162, 166–187.